The origin of cold gas in giant elliptical galaxies and its role in fuelling radio-mode AGN feedback

N. Werner,[1,2]★ J. B. R. Oonk,[3] M. Sun,[4] P. E. J. Nulsen,[5] S. W. Allen,[1,2,6]
R. E. A. Canning,[1,2] A. Simionescu,[7] A. Hoffer,[8] T. Connor,[8] M. Donahue,[8]
A. C. Edge,[9] A. C. Fabian,[10] A. von der Linden,[1,2,11] C. S. Reynolds[12]
and M. Ruszkowski[13,14]

[1]*Kavli Institute for Particle Astrophysics and Cosmology, Stanford University, 452 Lomita Mall, Stanford, CA 94305-4085, USA*
[2]*Department of Physics, Stanford University, 382 Via Pueblo Mall, Stanford, CA 94305-4060, USA*
[3]*ASTRON, Netherlands Institute for Radio Astronomy, PO Box 2, NL-7990 AA Dwingeloo, the Netherlands*
[4]*Department of Physics, University of Alabama in Huntsville, Huntsville, AL 35899, USA*
[5]*Harvard–Smithsonian Center for Astrophysics, 60 Garden Street, Cambridge, MA 02138, USA*
[6]*SLAC National Accelerator Laboratory, 2575 Sand Hill Road, Menlo Park, CA 94025, USA*
[7]*Institute of Space and Astronautical Science (ISAS), JAXA, 3-1-1 Yoshinodai, Chuo-ku, Sagamihara, Kanagawa, 252-5210 Japan*
[8]*Physics & Astronomy Department, Michigan State University, East Lansing, MI 48824-2320, USA*
[9]*Institute for Computational Cosmology, Department of Physics, Durham University, Durham DH1 3LE, UK*
[10]*Institute of Astronomy, Madingley Road, Cambridge CB3 0HA, UK*
[11]*Dark Cosmology Centre, Niels Bohr Institute, University of Copenhagen, Juliane Maries Vej 30, DK-2100 Copenhagen, Denmark*
[12]*Department of Astronomy and the Maryland Astronomy Center for Theory and Computation, University of Maryland, College Park, MD 20742, USA*
[13]*Department of Astronomy, University of Michigan, 500 Church Street, Ann Arbor, MI 48109, USA*
[14]*Michigan Center for Theoretical Physics, 3444 Randall Lab, 450 Church St, Ann Arbor, MI 48109, USA*

ABSTRACT

The nature and origin of the cold interstellar medium (ISM) in early-type galaxies are still a matter of debate, and understanding the role of this component in galaxy evolution and in fuelling the central supermassive black holes requires more observational constraints. Here, we present a multiwavelength study of the ISM in eight nearby, X-ray and optically bright, giant elliptical galaxies, all central dominant members of relatively low-mass groups. Using far-infrared spectral imaging with the *Herschel* Photodetector Array Camera & Spectrometer, we map the emission of cold gas in the cooling lines of [C II]λ157 µm, [O I] λ63 µm and [O Ib] λ145 µm. Additionally, we present Hα+[N II] imaging of warm ionized gas with the Southern Astrophysical Research (SOAR) telescope, and a study of the thermodynamic structure of the hot X-ray emitting plasma with *Chandra*. All systems with extended Hα emission in our sample (6/8 galaxies) display significant [C II] line emission indicating the presence of reservoirs of cold gas. This emission is cospatial with the optical Hα+[N II] emitting nebulae and the lowest entropy soft X-ray emitting plasma. The entropy profiles of the hot galactic atmospheres show a clear dichotomy, with the systems displaying extended emission-line nebulae having lower entropies beyond $r \gtrsim 1$ kpc than the cold-gas-poor systems. We show that while the hot atmospheres of the cold-gas-poor galaxies are thermally stable outside of their innermost cores, the atmospheres of the cold-gas-rich systems are prone to cooling instabilities. This provides considerable weight to the argument that cold gas in giant ellipticals is produced chiefly by cooling from the hot phase. We show that cooling instabilities may develop more easily in rotating systems and discuss an alternative condition for thermal instability for this case. The hot atmospheres of cold-gas-rich galaxies display disturbed morphologies indicating that the accretion of clumpy multiphase gas in these systems may result in variable power output of

★ E-mail: norbertw@stanford.edu

the AGN jets, potentially triggering sporadic, larger outbursts. In the two cold-gas-poor, X-ray morphologically relaxed galaxies of our sample, NGC 1399 and NGC 4472, powerful AGN outbursts may have destroyed or removed most of the cold gas from the cores, allowing the jets to propagate and deposit most of their energy further out, increasing the entropy of the hot galactic atmospheres and leaving their cores relatively undisturbed.

Key words: galaxies: active – galaxies: elliptical and lenticular, cD – galaxies: ISM – infrared: galaxies – X-rays: galaxies.

1 INTRODUCTION

Recent observations and simulations strongly suggest that the growth and evolution of giant early-type galaxies is closely tied to that of their central supermassive black holes through a well-regulated feedback cycle (e.g. Magorrian et al. 1998; Silk & Rees 1998; Croton et al. 2006; Sijacki et al. 2007). Many fundamental aspects of this feedback process, such as the nature of the material feeding the black holes in active galactic nuclei (AGN), jet formation and the heating, cooling and detailed physics of the interstellar medium (ISM) are not well understood. Among the best laboratories to test theories for the formation and growth of massive galaxies are nearby giant ellipticals, groups and clusters of galaxies: systems where hot X-ray emitting plasma may be cooling and accreting on to the galaxies and interacting with their AGN.

In massive galaxy clusters, with central cooling times shorter than the Hubble time, the central brightest cluster galaxies (BCG) are often surrounded by spectacular, filamentary optical Hα+[N II] emission-line nebulae extending up to 70 kpc from the core of the BCG (e.g. Cowie et al. 1983; Johnstone, Fabian & Nulsen 1987; Heckman et al. 1989; Donahue, Stocke & Gioia 1992; Crawford et al. 1999; McDonald et al. 2010). These nebulae of ionized gas seem to be cospatial with warm (1000–2000 K) molecular hydrogen seen in the near-infrared (e.g. Jaffe & Bremer 1997; Falcke et al. 1998; Donahue et al. 2000; Edge et al. 2002; Hatch et al. 2005; Jaffe, Bremer & Baker 2005; Johnstone et al. 2007; Oonk et al. 2010; Lim et al. 2012) and with large quantities (10^8–$10^{11.5}$ M$_\odot$) of cold (<50 K) molecular gas traced by CO (e.g. Edge 2001; Edge & Frayer 2003; Salomé & Combes 2003; McDonald, Wei & Veilleux 2012). Recently, observations with the *Herschel Space Observatory* (Pilbratt et al. 2010) also revealed the presence of far-infrared (FIR) cooling lines of [C II], [O I] and [N II] in the X-ray bright cores of Abell 1068, Abell 2597 (Edge et al. 2010), and the Centaurus, Perseus and Virgo clusters (Mittal et al. 2011, 2012; Werner et al. 2013). In nearby systems, such as the Centaurus, Perseus and Virgo clusters, where the spatial distribution of the [C II] line could be mapped, it was found to be extended and cospatial with optical Hα+[N II], far-ultraviolet C IV (in M 87, Sparks et al. 2012) and soft X-ray emission. The filamentary nebulae in the centres of massive cool-core galaxy clusters thus contain multiphase material spanning a temperature range of over five orders of magnitude, from <50 K to $\sim10^7$ K. This gas often appears to be interacting with the jets and the buoyant relativistic plasma from the central AGN (Fabian et al. 2003; Hatch et al. 2006; Canning et al. 2013). Despite the large quantities of cold gas, many extended nebulae show no evidence for recent star-formation.

The majority of AGN in these systems are in a quiescent, so called radio mode, where they are accreting at a modest rate. The accretion flows in this mode, though optically faint, often drive powerful relativistic jets, extending to large distances, which can have a profound impact on their surroundings. Using *Chandra* X-ray observations of nine nearby, X-ray luminous elliptical galaxies, Allen et al. (2006) found a tight correlation between

the Bondi accretion rates (see Bondi 1952) from the hot X-ray emitting ISM and the power in the relativistic jets (though see Russell et al. 2013b). The jet powers were determined from the work required to inflate bubbles of relativistic plasma associated with the most recent cavities in the hot X-ray emitting atmospheres of the galaxies (Churazov et al. 2002). The relationship between jet power and accretion rate of the hot ISM, however, raises the question: What is the role of the cold gas in the AGN feedback cycle?

Here, we present a multiwavelength study of eight nearby, X-ray bright, giant elliptical galaxies, all central dominant members of relatively low-mass groups. We use FIR data obtained with the *Herschel* Photodetector Array Camera & Spectrometer (PACS) in the lines of [C II] $\lambda157$ μm, [O I] $\lambda63$ μm and [O Ib] $\lambda145$ μm that are excellent probes of cold ~100 K gas; optical data from the Southern Astrophysical Research (SOAR) telescope in the lines of Hα+[N II] probing warm, ionized $\sim10\,000$ K gas; and X-ray data from the *Chandra X-ray Observatory*, tracing the hot 5–20 million K plasma permeating these systems.

1.1 The galaxy sample

Our target list is drawn from the parent sample of Dunn et al. (2010), who identified the optically and X-ray brightest giant elliptical/S0 galaxies within a distance $d \leq 100$ Mpc and with declination Dec. ≥ -45. Motivated by the goal of studying the properties of cold gas in these types of systems in detail, we selected only those galaxies with distance $d < 35$ Mpc and with relatively bright Hα+[N II] emission as reported by Macchetto et al. (1996). All of the systems in our sample are the central dominant galaxies of their respective groups. The properties of the galaxies are summarized in Table 1. The table lists the distances of the galaxies (Tonry et al. 2001; Blakeslee et al. 2009), their K-band near-infrared luminosities determined using the magnitudes measured by the 2MASS survey (Jarrett et al. 2003), Hα+ [N II] luminosities (Macchetto et al. 1996), radio luminosities at 1.4 GHz (Condon et al. 1998, 2002), bolometric X-ray luminosities (O'Sullivan et al. 2001), jet powers (Allen et al. 2006; Shurkin et al. 2008; David et al. 2009; Randall et al. 2011) and star-formation rates (SFRs) estimated using a combination of far-ultraviolet (FUV) data from *GALEX* and mid-infrared (MIR) data from *WISE*, employing the technique developed by Hao et al. (2011).

The near-infrared K-band luminosities, and by implication the stellar masses, span a range of approximately a factor of 3, with NGC 4636 being the least and NGC 4472 the most luminous. The Hα+[N II] luminosities span a range of a factor of 8, with NGC 5044 being the most luminous, and with NGC 4636 and NGC 4472 on the low-luminosity end. NGC 5044 boasts a particularly spectacular network of radial filaments, extending out to a radius of at least $r \sim10$ kpc (Gastaldello et al. 2009; David et al. 2011). The SFRs are small, typically of the order of 0.1 M$_\odot$ yr^{-1}, and they do not correlate with the Hα luminosities. All eight galaxies have central,

Table 1. Summary of the sample of galaxies. The distances in column 2 are from †Tonry et al. (2001) and ‡Blakeslee et al. (2009). The *K*-band luminosities in column 5 were determined using the 2MASS survey (Jarrett et al. 2003). The Hα+[N II] luminosities in column 6 are from Macchetto et al. (1996). The luminosities marked with '⋆' have been revised in Section 3 and Table 4. The 1.4 GHz radio luminosities in column 7 are from Condon et al. (1998) and Condon, Cotton & Broderick (2002). Bolometric X-ray luminosities in column 8 are from O'Sullivan, Forbes & Ponman (2001). The jet powers for NGC 4636, NGC 4472 and NGC 5846 are from Allen et al. (2006), for NGC 5044 from David et al. (2009), for NGC 1399 from Shurkin et al. (2008) and for NGC 5813 from Randall et al. (2011). For the jet powers in NGC 5044 and NGC 5813 no error bars were published (Randall et al. 2011; David et al. 2009). Star formation rates were estimated using a combination of FUV data from *GALEX* and MIR data from *WISE*, employing the technique developed by Hao et al. (2011).

Galaxy	d (Mpc)	Scale (arcsec kpc^{-1})	z	L_K ($\times 10^{40}$ erg s^{-1})	$L_{H\alpha+[N\,II]}$ ($\times 10^{39}$ erg s^{-1})	L_{radio} ($\times 10^{38}$ erg s^{-1})	L_X ($\times 10^{41}$ erg s^{-1})	P_{jet} ($\times 10^{41}$ erg s^{-1})	SFR M$_\odot$ yr^{-1}
NGC 1399	20.9‡	9.9	0.004 753	2.69	9.3⋆	1.52	5.68	21.9 ± 7	0.171
NGC 4472	16.7‡	12.4	0.003 326	3.97	5.8	1.20	2.96	80.7 ± 23.5	0.099
NGC 4636	14.7†	14.0	0.003 129	1.20	5.5⋆	0.28	3.32	3.0 ± 0.8	0.027
NGC 5044	31.2†	6.6	0.009 280	1.65	45.6⋆	0.59	5.87	6.0	0.073
NGC 5813	32.2†	6.4	0.006 578	2.30	14.0⋆	0.26	10.63	1.2	0.063
NGC 5846	27.1†	7.6	0.005 717	2.11	24.6	0.26	6.25	7.4 ± 2.6	0.074
NGC 6868	26.8†	5.6	0.009 520	1.74	23.8	1.00	1.01	−	0.078
NGC 7049	29.9†	7.1	0.007 622	2.32	31.8	0.84	1.23	−	0.117

active radio jets, also spanning a range of radio luminosities and jet powers. The X-ray luminosities of the galaxies span a range of an order of magnitude.

2 OBSERVATIONS AND DATA ANALYSIS

2.1 FIR spectroscopy with *Herschel* PACS

We observed the FIR cooling lines of [C II] λ157 μm, [O I] λ63 μm and [O Ib] λ145 μm in our sample of eight galaxies with the PACS integral-field spectrometer (Poglitsch et al. 2010) on the *Herschel Space Observatory*. Table 2 gives a summary of the observations. The observations were taken in line spectroscopy mode with chopping-nodding to remove the telescope background, sky background and dark current. A chopper throw of 6 arcmin was used. For seven systems, with a relatively compact Hα emission region, the observations were taken in pointed mode targeting the centres of the

galaxies. For NGC 5044, we used raster mapping in 3 × 3 steps of 23.5 arcsec to match the extent of the Hα nebula. The observations were reduced using the HIPE software version 8.2.0, using the PACS `ChopNodLineScan` pipeline script. This script processes the data from level 0 (raw channel data) to level 2 (flux-calibrated spectral cubes).

During the final stage of the reduction the data were spectrally and spatially rebinned into 5 × 5 × λ cubes. In the following, we will refer to these cubes as the rebinned cubes. Each spatial pixel, termed spaxel, in these cubes has a size of 9.4 × 9.4 arcsec^2. The cubes thus provide us with a field of view (FoV) of 47 × 47 arcsec^2. For the wavelength regridding, the parameters `oversample` and `upsample` were set to 2 and 1, respectively. This means that one spectral bin corresponds to the native resolution of the PACS instrument.

The integrated [C II] line fluxes were in all cases, except for NGC 5044, obtained by spatially integrating the 5 × 5 spaxels from the rebinned cubes. For NGC 5044 the integrated line flux is obtained after projecting the individual rebinned cubes on to the sky. No point

Table 2. Summary of observations.

Galaxy	*Herschel* obs. ID	*Herschel* exp. (s)	*Chandra* obs. ID	Detector	*Chandra* exp. (ks)	SOAR/SOI obs. date	SOAR/SOI filter	SOAR/SOI exp (s)
NGC1399	1342239492	8161	319	ACIS-S	49.9	2012 Oct. 9	CTIO 656375-4/6916-78	3 × 600 / 3 × 600
			4172	ACIS-I	36.7	2013 Aug. 4	Goodman 1.68 arcsec long slit, KOSI600 grating	3 × 480
			9530	ACIS-S	59.3	2013 Sep. 8	Goodman 3.0 arcsec long slit, KOSI600 grating	4 × 480
NGC4472	1342234992	8161	321	ACIS-S	19.1			
NGC4636	1342236884	5442	323	ACIS-S	35.8	2009 June 1	CTIO 6600/75	3 × 780
							CTIO 6120/140	3 × 500
NGC5044	1342238376	24723	9399	ACIS-S	53.4	2010 April 10	CTIO 6649/76	3 × 1200
			3926	ACIS-I	54.5		CTIO 6520/76	3 × 720
			4415	ACIS-I	73.3			
NGC5813	1342238158	10880	5907	ACIS-S	47.4	2008 July 6	CTIO 6600/75	3 × 900
			9517	ACIS-S	98.8		CTIO 6120/140	3 × 720
NGC5846	1342238157	5442	788	ACIS-S	17.3	2009 June 1	CTIO 6600/75	3 × 900
			7923	ACIS-I	75.9		CTIO 6120/140	3 × 540
NGC6868	1342215929	5442	3191	ACIS-I	18.6	2012 Oct. 9	CTIO 6600/75	2 × 900, 1 × 600
			11753	ACIS-I	56.8	2012 Oct. 9	CTIO 6563/75	2 × 900, 1 × 600
NGC7049	1342216658	5442	5895	ACIS-I	2.2	2012 Oct. 9	CTIO 6600/75	2 × 900, 1 × 600
						2012 Oct. 9	CTIO 6563/75	1 × 900, 2 × 600

spread function (PSF) correction is applied as the [C II] emission, in all cases where it is detected, is found to be extended.

To visualize the extent of the [C II] emission in our galaxies, we have created sky maps of the [C II] emission by using the specProject task in HIPE and the hrebin task in IDL. In the following, we will refer to these data cubes as the projected cubes. A pixel size of 6 arcsec was chosen in order to Nyquist sample the beam, the full width at half-maximum (FWHM) of which is 12 arcsec at the observed wavelength of the [C II] line. We only consider spatial bins where the signal-to-noise ratio of the integrated line flux is greater than 2. We have compared the integrated line fluxes obtained from the level 2 rebinned cubes with those from the projected cubes and find that they are consistent. Velocity and velocity width maps were constructed by fitting a single Gaussian to the projected data.

For the [O I] and [O Ib] lines, we report line fluxes obtained from either the central spaxel or the central 3×3 spaxels. The PSF corrected fluxes should be viewed as lower limits to the true [O I] and [O Ib] line emission in these galaxies. For NGC 5044, the integrated [O I] and [O Ib] fluxes are obtained after projecting the individual rebinned cubes on to the sky.

2.2 Hα+[N II] imaging and spectroscopy

We performed narrow-band imaging observations for all systems in our sample, except for NGC 4472, using the SOAR Optical Imager (SOI) on the 4.1 m SOAR telescope. See Table 2 for details on the observations. For each galaxy, we obtained two narrow-band images, one centred on the Hα emission and the other in an adjacent emission-line free band. We reduced the images using standard procedures in the IRAF MSCRED package. The pixels were binned by a factor of 2, for a scale of 0.154 arcsec per pixel. The typical seeing was ~1 arcsec. Spectrophotometric standard stars were observed for each exposure. More detail on the SOI data reduction can be found in Sun, Donahue & Voit (2007). For continuum subtraction, we follow the isophote fitting method described in Goudfrooij et al. (1994). We assumed line ratios of [N II]λ6583/Hα = 1.5 and [N II] λ6548/[N II] λ6583 = 1/3, which are consistent with the typical values in Goudfrooij et al. (1994).

On 2013 August 4 and September 8, we also took spectra of NGC 1399 using the Goodman spectrograph on the SOAR telescope. We used a 600 lines per mm grating for the wavelength range of 4350–6950 Å. The first run was taken with a 1.68 arcsec slit, along the NS direction. The second run was taken with a 3.0 arcsec slit, at a position angle of 302° (almost along the major axis of the galaxy). We took three 480 s exposures on the first night and four 480 s exposures on the second night. Before and after each exposure, we took a quartz flat and a comparison spectrum of an Fe lamp. Bias correction, flat-fielding and wavelength calibration were all performed using standard IRAF procedures. For flux calibration, we took spectra of the spectrophotometric standard stars LTT7379 and LTT1020.

2.3 *Chandra* X-ray data

The archival *Chandra* data were reprocessed using the CIAO (version 4.3) software package. We cleaned the data to remove periods of anomalously high background. Table 2 summarizes the net exposure times after cleaning. Our data reduction procedures are described in detail in Million et al. (2010a,b).

To produce 2D maps of projected thermodynamic quantities, we identified spatial regions using the contour binning algorithm (Sanders 2006), which groups neighbouring pixels of similar surface brightness until a desired signal-to-noise ratio threshold is met. We

adopted a signal-to-noise ratio of 18–25 (~320–630 counts per region) in the 0.6–2.0 keV band, which gives us small enough regions to resolve substructure, yet provides enough counts to achieve better than 5 per cent precision on the temperature. Point sources were identified using the CIAO task WAVDETECT and excluded from all regions used for spectral analysis. Separate photon-weighted response matrices and effective area files were constructed for each spectral region.

We modelled the spectra extracted from each spatial region with the SPEX package (Kaastra, Mewe & Nieuwenhuijzen 1996). The spectrum for each region was fitted with a model consisting of an absorbed single-phase plasma in collisional ionization equilibrium, with the temperature and spectral normalization (emission measure) as free parameters. The line-of-sight absorption column densities, $N_{\rm H}$, were fixed to the values determined by the Leiden/Argentine/Bonn radio survey of H I (Kalberla et al. 2005).

From the best-fitting emission measures, $Y = \int n_{\rm H} n_{\rm e} dV$, where $n_{\rm H} = n_{\rm e}/1.2$ is the hydrogen number density and V is the emitting plasma volume, we determined the projected electron densities, $n_{\rm e}$, for each region assuming a fixed column depth of $l = 20$ kpc. Using these electron densities and the best-fitting plasma temperatures (kT), we determined the pressures ($P_{\rm e} = n_{\rm e}kT$) and entropies ($K = kT/n_{\rm e}^{2/3}$). We note that the choice of the assumed column depth for these projected maps is arbitrary and it does not affect the magnitude of the observed azimuthal variations in the derived thermodynamic properties.

Because the statistical quality of the data for the X-ray faintest galaxies in our sample, NGC 6868 and NGC 7049, does not allow us to produce 2D maps of thermodynamic properties, we only present X-ray images for these systems. Background-subtracted images were created in six narrow energy bands, spanning 0.5–2.0 keV. These were flat fielded with respect to the median energy for each image and then co-added to create the broad-band X-ray images.

To determine the deprojected thermodynamic properties of the hot gas, we extracted, for each galaxy (except NGC 7049), a set of azimuthally averaged spectra from concentric annuli. We modelled these spectra simultaneously in the 0.6–2.0 keV band, with the XSPEC (version 12.5 Arnaud 1996) spectral fitting package, using PROJCT model (see Werner, Allen & Simionescu 2012, for details). We have determined the azimuthally averaged deprojected radial profiles of electron density and temperature, from which we derived the deprojected radial profiles for entropy, electron pressure and cooling time. We define the cooling time as the gas enthalpy divided by the energy radiated per unit volume of the plasma:

$$t_{\rm cool} = \frac{\frac{5}{2}(n_{\rm e} + n_{\rm i})kT}{n_{\rm e}n_{\rm i}\Lambda(T)}, \tag{1}$$

where the ion number density $n_{\rm i} = 0.92 n_{\rm e}$, and $\Lambda(T)$ is the cooling function for Solar metallicity tabulated by Schure et al. (2009). We caution that, because the deprojected thermodynamic properties are determined assuming spherical symmetry, for the 5/7 analysed galaxies with disturbed morphologies, the derived values have significant systematic uncertainties.

3 RESULTS

Using *Herschel* PACS, we detect FIR [C II] λ157 µm line emission in 7/8 systems (see Fig. A1 and Table 3). The detections of [O I] λ63.2 µm and [O Ib] λ145.5 µm lines are relatively weak, and are only seen in 4/8 and 3/8 systems, respectively (see Fig. A2, A3 and Table 3). No cold gas is detected in NGC 1399 and the [C II] detection in NGC 4472 is relatively weak. Table 3 lists the observed

Table 3. Summary of observations with *Herschel* PACS and the properties of the FIR lines.

Galaxy	Line	Observation duration (s)	Line flux in central spaxel (10^{-14} erg s^{-1} cm^{-2})	Observed FWHM (km s^{-1})	Line shift (km s^{-1})	Integrated line flux (10^{-14} erg s^{-1} cm^{-2})
NGC 1399	C II λ157.7 μm	2250	<0.2	300*	–	–
	O I λ63.2 μm	2484	<2.8	300*	–	–
	O Ib λ145.5 μm	3360	<0.2	300*	–	–
NGC 4472	C II λ157.7 μm	2250	0.2 ± 0.04	255 ± 36	99 ± 15	1.04 ± 0.16
	O I λ63.2 μm	2484	<2.5	255*	–	–
	O Ib λ145.5 μm	3360	<0.2	255*	–	–
NGC 4636	C II λ157.7 μm	1500	2.6 ± 0.06	361 ± 6	22 ± 3	10.52 ± 0.37
	O I λ63.2 μm	1656	1.3 ± 0.2 (1.9)	233 ± 29	75 ± 12	–
	O Ib λ145.5 μm	2240	<0.5	233*	–	–
NGC 5044	C II λ157.7 μm	6750	–	–	–	31.73 ± 4.76
	O I λ63.2 μm	7452	–	–	–	7.1 ± 1.8
	O Ib λ145.5 μm	10 080	–	–	–	1.0 ± 0.5
NGC 5813	C II λ157.7 μm	3000	1.4 ± 0.04	419 ± 10	96 ± 4	8.55 ± 0.26
	O I λ63.2 μm	3312	1.0 ± 0.2 (1.5)	273 ± 36	30 ± 15	–
	O Ib λ145.5 μm	4480	0.2 ± 0.04 (0.4)	608 ± 88	100 ± 37	1.4 ± 0.2
NGC 5846	C II λ157.7 μm	1500	2.2 ± 0.06	477 ± 10	−25 ± 4	13.61 ± 0.36
	O I λ63.2 μm	1656	<2.5	477*	–	–
	O Ib λ145.5 μm	2240	<0.3	477*	–	–
NGC 6868	C II λ157.7 μm	1500	5.7 ± 0.08	510 ± 6	125 ± 3	21.61 ± 0.44
	O I λ63.2 μm	1656	3.0 ± 0.3	506 ± 31	137 ± 13	5.9 ± 0.8
	O Ib λ145.5 μm	2240	0.5 ± 0.06	579 ± 50	125 ± 21	2.0 ± 0.3
NGC 7049	C II λ157.7 μm	1500	2.5 ± 0.06	395 ± 7	78 ± 3	22.49 ± 0.45
	O I λ63.2 μm	1656	<3.3	395*	–	–
	O Ib λ145.5 μm	2240	<0.2	395*	–	–

Notes. In parentheses, we indicate the PSF-corrected fluxes determined assuming the emission comes from a point source, correcting the measured spaxel flux upward to account for the beam size. The PSF corrected fluxes can therefore be considered a lower limit to the flux integrated over the whole PACS area.
*indicates the velocity widths are assumed to be equal to the FWHM of the [CII] line. For NGC 1399 we assumed a FWHM = 300 km s^{-1}.

lines for all the target galaxies, their rest-frame wavelengths and observation durations. For the central spaxel, we present the observed line fluxes and the 2σ upper limits where appropriate, the observed FWHM, and the observed line shifts with respect to the systemic velocity determined based on optical data. In the parentheses, we give the PSF corrected fluxes determined assuming that the emission comes from a point source, correcting the measured spaxel flux upwards to account for the beam size. The PSF-corrected fluxes can therefore be considered a lower limit to the flux integrated over the whole PACS area. For sources that allow us to confirm that the emission is extended we report non-PSF-corrected fluxes. The last column gives the line fluxes spatially integrated over the 5 × 5 spaxel (47 arcsec × 47 arcsec) *Herschel* PACS FoV.

The [O I]/[C II] line ratios determined from the central spaxel in systems with significant [O I] detections are in the range of 0.4–0.8. The 2σ upper limits on the fluxes of the [O I] λ63 μm and [O Ib] λ145 μm lines given in Table 3 were determined assuming that their velocity widths are equal to the FWHM of the [C II] line.

As indicated in Section 1.1 and in Table 1, according to Macchetto et al. (1996) all our targets are Hα luminous. Fig. 1 shows narrow-band Hα+[N II] images obtained with the SOAR telescope of our six targets with extended line-emitting nebulae. The nebulae in NGC 6868 and NGC 7049 show regular extended disc-like morphologies reaching radii $r \sim$ 2–3 kpc (see also Macchetto et al. 1996). On the other hand, NGC 5044, NGC 5813, NGC 5846 and NGC 4636 show filamentary emission. NGC 5044 has the largest optical emission-line luminosity, with a rich, dense network of filaments extending from the core out to a radius of ∼10 kpc (see also Gastaldello et al. 2009; David et al. 2011). The nebulae in NGC 5813 show a radial bipolar distribution in the direction of buoyant bubbles rising in the hot X-ray emitting atmosphere of the galaxy (see also Randall et al. 2011). The bright Hα+[N II] emission in NGC 4636 and NGC 5846

appears relatively compact, concentrated in the innermost $r \lesssim$ 1.5 kpc of the galaxies, but the morphology of the nebulae is clearly filamentary exhibiting signs of interaction with the central AGN.

Our new SOAR data allow robust constraints on the Hα+[N II] flux in four galaxies, NGC 5044, NGC 4636, NGC 5813 and NGC 1399 (see Table 4). The NGC 5846 data were not taken in photometric conditions, and for NGC 6868 and NGC 7049, the filters available at the time of the observations made the continuum subtraction less reliable than what is achieved for other galaxies. Our Hα+[N II] flux for NGC 4636 is consistent with the values published by Macchetto et al. (1996) and Buson et al. (1993). For NGC 5813, our result is consistent with Goudfrooij et al. (1994) but is almost a factor of 2 higher than the flux measured by Macchetto et al. (1996). For NGC 5044, our flux is significantly higher than the values measured by Goudfrooij et al. (1994) and Macchetto et al. (1996), but is consistent with the result of Rickes, Pastoriza & Bonatto (2004). The large spatial extent of the nebula surrounding NGC 5044 combined with the small FoV of the instrument (1.4 arcmin× 2.2′ arcmin) may have prevented Macchetto et al. (1996) from a robust determination of the local background.

Contrary to the results of Macchetto et al. (1996), we detected no Hα+[N II] emission in NGC 1399. Goudfrooij et al. (1994) derived an Hα+[N II] flux of $4.2 \pm 0.2 \times 10^{-14}$ erg s^{-1} cm^{-2}, much smaller than the value measured by Macchetto et al. (1996). Our SOI Hα+[N II] imaging analysis of NGC 1399, with either adjacent narrow-band or *R*-band image for the continuum subtraction, results in negative net flux around the centre of the galaxy, indicative of Hα absorption. Therefore, we took additional long-slit spectra with the Goodman spectrograph on SOAR. Our Goodman spectra give a 5σ limit on the EW of the emission line of 0.1 Å. Assuming that all the Hα+[N II] emission is from the central 12 arcsec radius, as shown by the Hα+[N II] image from Macchetto et al.

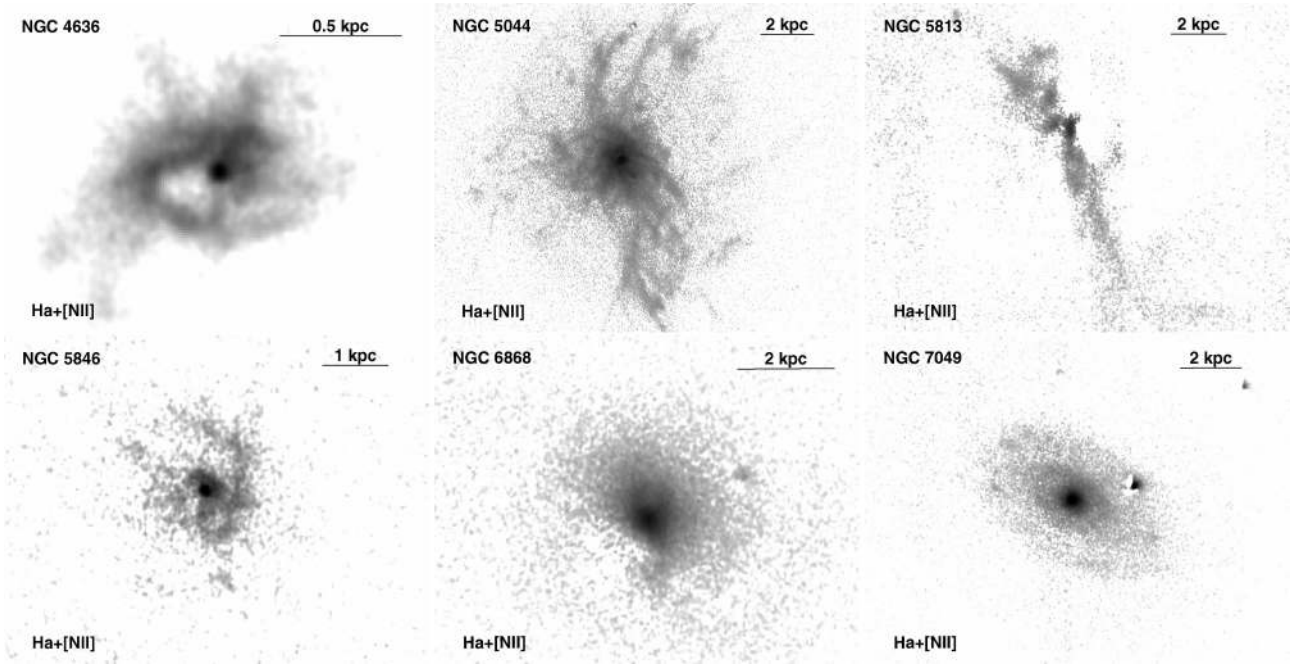**Figure 1.** Hα+[N ɪɪ] images of the galaxies with extended emission-line nebulae in our sample obtained with the 4.1 m SOAR telescope.

Table 4. Hα+[N ɪɪ] fluxes from the SOAR telescope.

Galaxy	$f_{Hα+[NII]}$ (10^{-13} erg s^{-1} cm^{-2})
NGC 1399	<0.34
NGC 4636	2.7 ± 0.4
NGC 5044	7.6 ± 0.9
NGC 5813	2.2 ± 0.3

(1996), this EW upper limit translates to an Hα+[N ɪɪ] flux limit of 3.4×10^{-14} erg s^{-1} cm^{-2}. The lack of a spectroscopic detection of optical emission lines in NGC 1399 is inconsistent with previous reports of detections through narrow-band filters. We suspect that the previously reported detections of morphologically smooth line emission, where the emitting region has the same morphology as the old stellar populations, may be due to colour gradients in the stellar population of the galaxy. Currently, we do not have SOAR data for NGC 4472.

In Fig. 2, we plot the Hα+[N ɪɪ] luminosities (bottom panel), 70/24 μm infrared continuum ratios (middle panel; Temi et al. 2007a) and the *K*-band luminosity (top panel, based on the 2MASS survey; Jarrett et al. 2003) against the spatially integrated [C ɪɪ] luminosity measured by *Herschel* PACS. The ratio of the [C ɪɪ] over Hα+[N ɪɪ] luminosity is remarkably similar ∼0.4–0.8 for 6/8 galaxies in our sample. For the same 6/8 systems, the [C ɪɪ] λ157 μm line emission is spatially extended and appears to follow the distribution of the Hα+[N ɪɪ] filaments (see the left-hand panels of Figs 4 and 5). In the extended network of filaments of NGC 5044 at $r \gtrsim 1$ kpc, the [C ɪɪ]/(Hα+[N ɪɪ]) ratios also remain similar as a function of position. In the two FIR faint systems (shown by the red data points), the ionized Hα emission is either concentrated in the nucleus of the galaxy (NGC 4472; Macchetto et al. 1996) or is not present (NGC 1399).

The [C ɪɪ] luminosities, which are likely excellent tracers of the cold molecular gas mass (Crawford et al. 1985), do not correlate

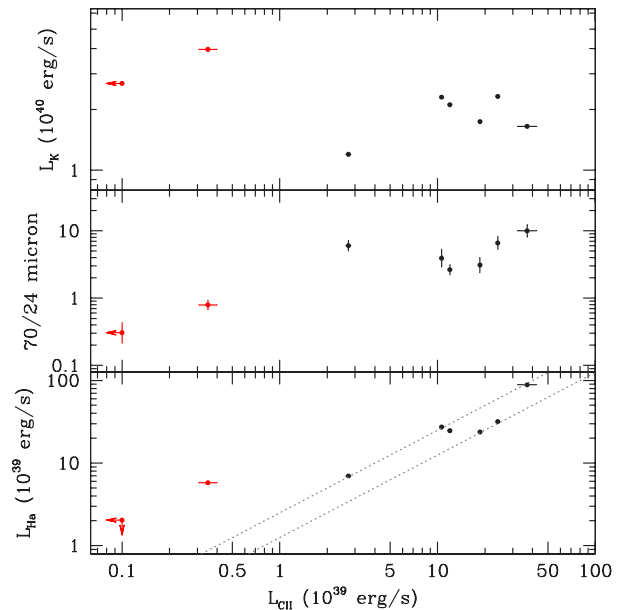**Figure 2.** The Hα+[N ɪɪ] luminosity (bottom panel) from SOAR for NGC 1399, NGC 5044, NGC 5813 and NGC 4636 (see Table 4) and from Macchetto et al. (1996) for NGC 4472, NGC 5846, NGC 6868 and NGC 7049 (see Table 1), 70/24 μm infrared continuum ratio (middle panel; Temi, Brighenti & Mathews 2007a), and *K*-band luminosity (top panel, based on the 2MASS survey; Jarrett et al. 2003) plotted against the spatially integrated [C ɪɪ] luminosity measured by *Herschel* PACS. The grey dotted lines in the bottom panel indicate constant [C ɪɪ] over Hα+[N ɪɪ] luminosity ratios of 0.4 and 0.8. These ratios are remarkably similar for 6/8 galaxies in our sample. The outliers, NGC 4472 and NGC 1399, have little or no cold gas. They are indicated in red.

with the *K*-band luminosities (see Table 1), which trace the stellar masses of the galaxies. There is also no correlation between the [C ɪɪ] luminosities of systems with extended emission-line nebulae and the 70/24 μm infrared continuum ratios. In the FIR faint systems
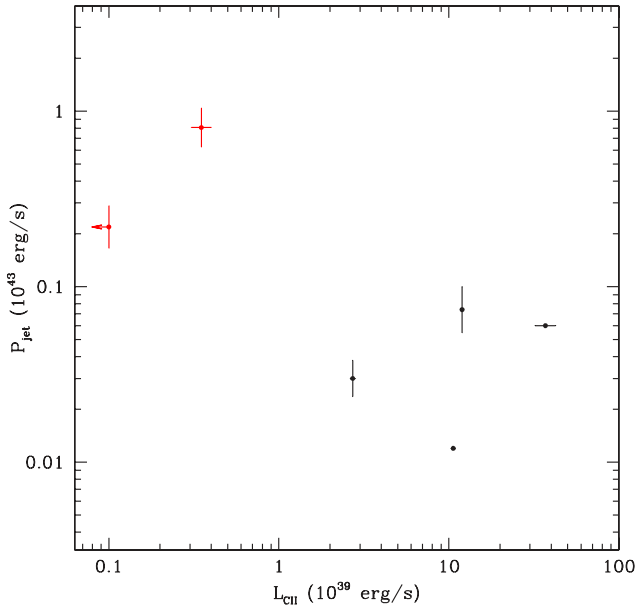
Figure 3. Jet powers (Allen et al. 2006; Shurkin et al. 2008; David et al. 2009; Randall et al. 2011) plotted against the spatially integrated [C II] luminosity measured by *Herschel* PACS. Galaxies with little or no cold gas are indicated in red. For the jet powers in NGC 5044 and NGC 5813 no error bars were published (David et al. 2009; Randall et al. 2011).

indicated by the red data points, these ratios are smaller (see the central panel of Fig. 2). The 70/24 μm infrared continuum ratio is a good tracer of interstellar dust (Temi et al. 2007a).

Fig. 3 shows that the [C II] luminosities in systems with spatially extended emission do not correlate with the jet powers determined from the work required to inflate bubbles of relativistic plasma associated with the cavities in the hot X-ray emitting atmospheres of the galaxies listed in Table 1. In our relatively small sample, the galaxies with little or no cold gas (indicated in red) have higher jet powers than the systems with significant [C II] detections.

The central panels of Figs 4 and 5 show the velocity distributions of the [C II] line emitting gas with respect to the velocities of the host galaxies. In NGC 6868 and NGC 7049, the velocity distribution of the [C II] emitting gas indicates that the cold gas forms a rotating disc. This is consistent with the overall morphology of the optical line emission nebulae. The velocity distribution of the [C II] emitting gas in the other four systems with extended emission does not show any coherent structure.

The projected velocity dispersions measured from the [C II] lines along our line of sight are generally in the range between 100 and 200 km s^{-1}, with the highest measured values reaching ~280 km s^{-1}.

Fig. 6 shows maps of the pressure and entropy in the hot X-ray emitting intragroup/interstellar medium for the galaxies where the cold gas has a filamentary morphology. In all of these systems, the filaments are cospatial with the lowest entropy hot X-ray emitting gas. They also appear to anticorrelate and interact with the AGN-inflated bubbles of relativistic plasma, which provide significant non-thermal pressure in the X-ray atmospheres of the galaxies and therefore appear as regions of low projected X-ray pressure on our maps. This is most clearly seen for the southwestern filament in NGC 5813, which appears to be pushed aside by the large, older, outer bubble. The inner portion of the filament also appears on the side and partly on the top of the small, younger, inner southwestern bubble that is currently being inflated in the core (for detailed

discussion on the bubbles, see Randall et al. 2011). Similar interaction, with the filaments being pushed around by the bubbles, is seen in NGC 5846 and NGC 4636, both of which show 'cavities' in the Hα+[N II] images that coincide with pressure decrements in their X-ray spectral maps. NGC 5044 shows a strongly disturbed morphology due to both AGN activity and the intragroup medium sloshing in the gravitational potential of the system (David et al. 2009, 2011; Gastaldello et al. 2009; O'Sullivan, David & Vrtilek 2013).

Fig. 7 shows the pressure and entropy maps for NGC 4472 and NGC 1399 – systems with little or no cold and warm gas. Compared to the systems with filamentary Hα nebulae, their thermodynamic maps have relatively regular morphologies. These systems are among the nearby giant ellipticals with the most relaxed X-ray morphologies at small radii (Werner et al. 2012).

NGC 6868 and NGC 7049 do not have X-ray data with the quality that would allow us to extract detailed maps of thermodynamic properties and in Fig. 8 we only show their X-ray images. The images show extended X-ray haloes, cospatial with the Hα+[N II] emission, surrounding the galaxies. The X-ray image of NGC 6868 shows a relatively complex disturbed morphology (see also Machacek et al. 2010). The X-ray data of NGC 7049 are very shallow and only allow us to detect the extended X-ray emission. Four galaxies – NGC 5044, NGC 6868, NGC 7049 and NGC 5813 – have an X-ray point source associated with the central AGN.

The deprojected central densities and pressures measured at $r = 0.5$ kpc in the morphologically relaxed NGC 1399 and NGC 4472 appear significantly higher than in the other, more disturbed, [C II] bright systems (see Table 5). All [C II] bright galaxies appear to have similar central densities and pressures. The entropies at $r = 0.5$ kpc span a small range of 3.0–4.5 keV cm^2 and the central cooling times are 4–8×10^7 yr. At radii $r \gtrsim 1$ kpc, the entropies of the galaxies containing cold gas (except NGC 6868) are systematically lower than those of NGC 1399 and NGC 4472 (see Fig. 9). The measured relatively low central densities and pressures of the morphologically disturbed systems may partly be due to the additional non-thermal pressure support in the central regions of the these systems. However, we also suspect a bias due to departures from spherical symmetry. Due to the non-uniform surface brightness within the circular annuli used in the deprojection analysis, densities in the outer shells may be somewhat overestimated, leading to underestimated central densities. For the morphologically disturbed systems, we repeated the deprojection analysis using wedges and found that despite the systematic uncertainties, at radii $r \gtrsim 1$ kpc, the difference in the shapes of the profiles shown in Fig. 9 remains robust.

4 DISCUSSION

4.1 Properties of the cold ISM

The observed high [C II] luminosities indicate the presence of large reservoirs of cold gas. Cold gas is evidently prevalent in massive giant elliptical galaxies with spatially extended Hα+[N II] nebulae, even though their stellar populations are old and appear red and dead (Annibali et al. 2007). NGC 5044 has previously also been detected in the CO(2–1) line with the 30 m IRAM telescope with a total flux of 6.6×10^{-17} erg s^{-1} cm^{-2} (Lim & Combes, private communication). Assuming a CO(2–1) to CO(1–0) ratio of 0.8, we obtain a [C II] λ158 μm over CO(1–0) flux ratio of 3817, which is within the range of the ratios (1500–6300) observed in normal and star-forming galaxies and in Galactic molecular clouds (Crawford et al. 1985; Stacey et al. 1991).
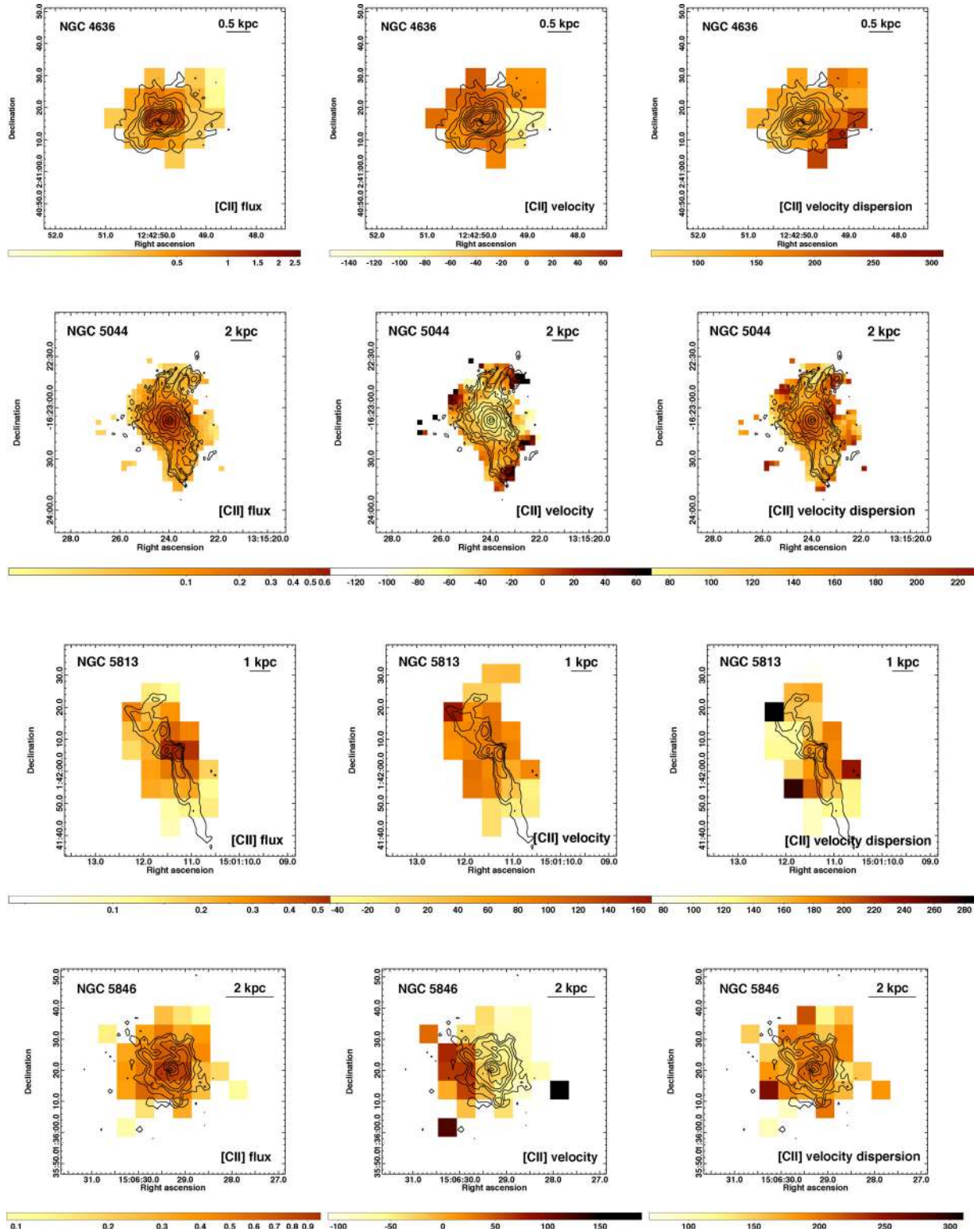
Figure 4. Left-hand panels: maps of the integrated [C II] line flux in units of 10^{-14} erg s^{-1} cm^{-2} per 6 arcsec × 6 arcsec spaxel obtained with *Herschel* PACS for NGC 4636, NGC 5044, NGC 5813 and NGC 5846. Central panels: the velocity distribution of the [C II] emitting gas, in units of km s^{-1}, relative to the systemic velocity of the host galaxy. Right-hand panels: map of the velocity dispersion, σ, of the [C II] emitting gas. Contours of the Hα+[N II] emission are overlaid.

Assuming the cold ~100 K [C II] emitting gas is in thermal pressure equilibrium with the surrounding hot X-ray emitting plasma, it will presumably form filaments with densities ~10^4 cm^{-3} and small volume filling fractions. As discussed in Fabian et al. (2003,

2008, 2011) and Werner et al. (2013), the emission-line filaments are likely to consist of many strands that have small volume filling fractions but large area covering factors. The soft X-ray emission that is always associated with filaments in cool-core clusters (Sanders &
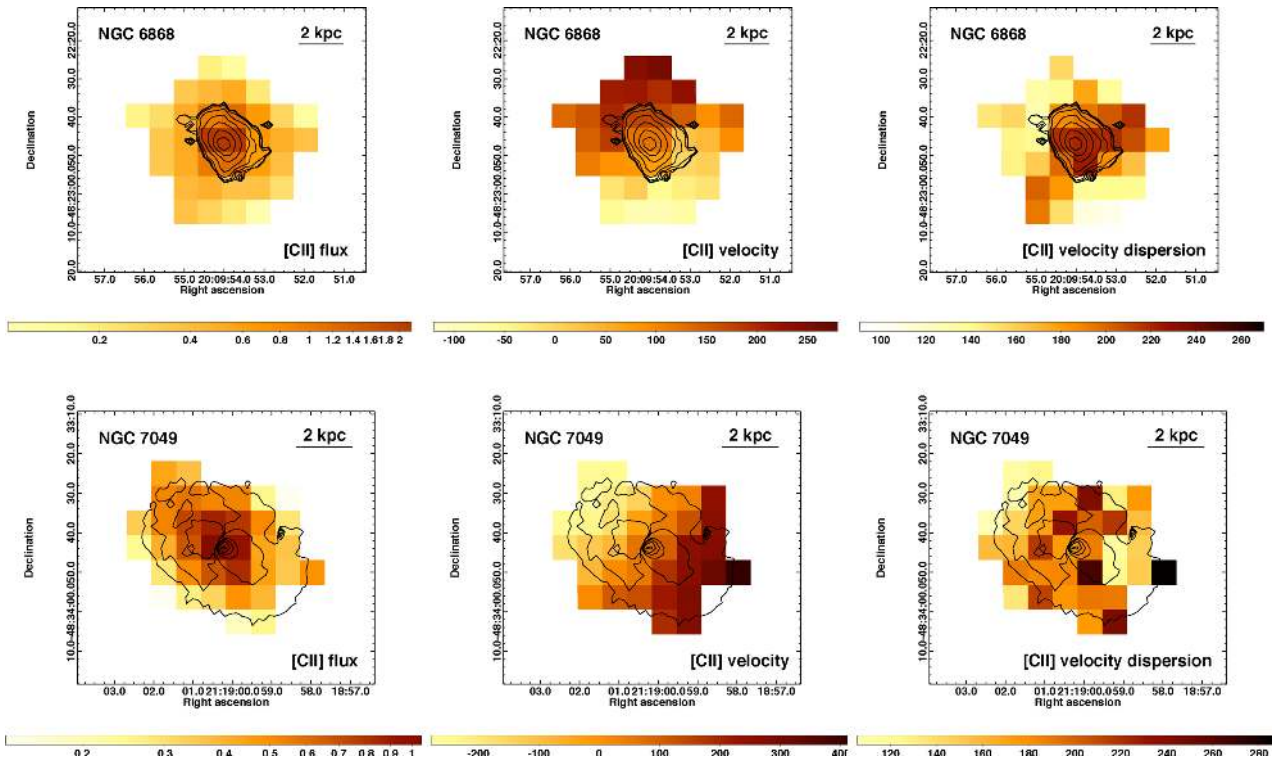
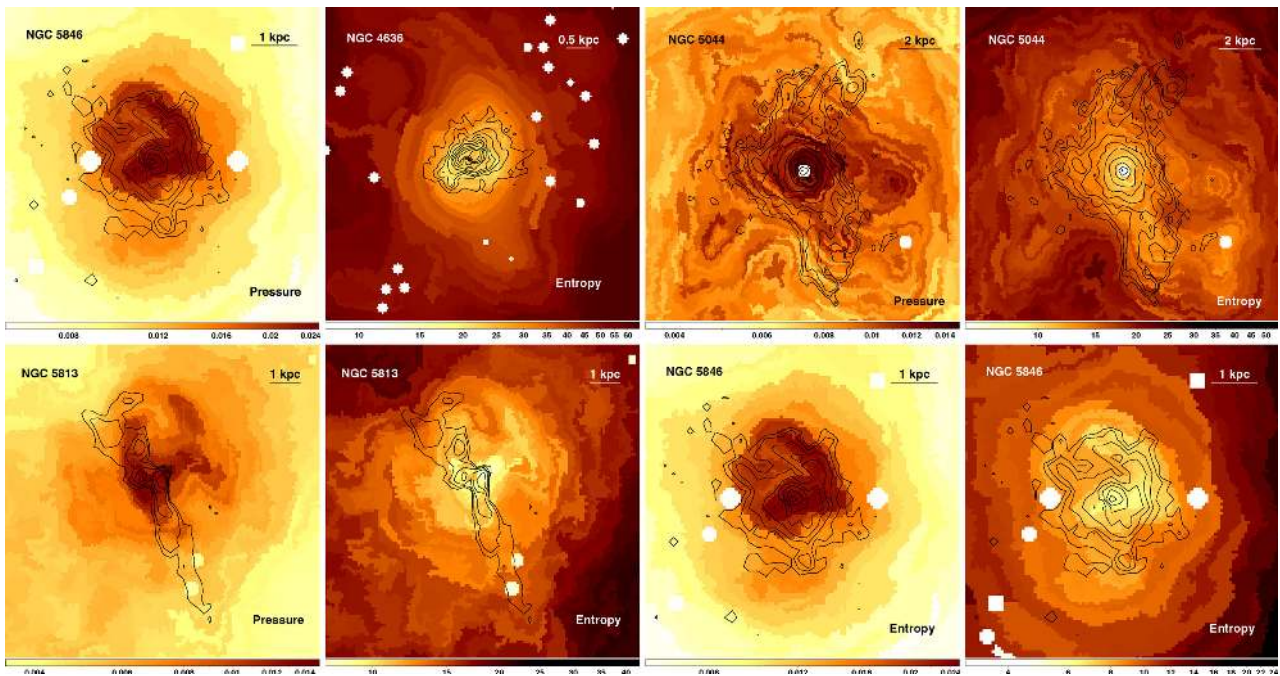**Figure 5.** Same as Fig. 4, but for NGC 6868 and NGC 7049.

Figure 6. 2D map of the hot gas pressure (in units of keV cm$^{-3} \times (\frac{l}{20\,\text{kpc}})^{-1/2}$) and entropy (in units of keV cm$^2 \times (\frac{l}{20\,\text{kpc}})^{1/3}$) with the H$\alpha$+[N II] contours overlaid. The maps were obtained by fitting each region independently with a single temperature thermal model, yielding 1σ fractional uncertainties of ∼3–5 per cent in temperature, entropy and pressure. Point sources were excluded from the spectral analysis and therefore appear as white circles on the maps.

Fabian 2007; Sanders et al. 2008, 2010; Sanders, Fabian & Taylor 2009; de Plaa et al. 2010; Werner et al. 2011, 2010, 2013) indicates the presence of cooling hot plasma distributed between the threads. The hot plasma may be cooling both radiatively and by mixing with the cold gas in the filaments. Part of the soft X-ray emission from

this cooling plasma gets absorbed by the cold gas in the strands (Werner et al. 2013).

The velocities inferred from the [C II] line emission are consistent with those measured from the Hα+[N II] lines by Caon, Macchetto & Pastoriza (2000), indicating that the different observed gas phases
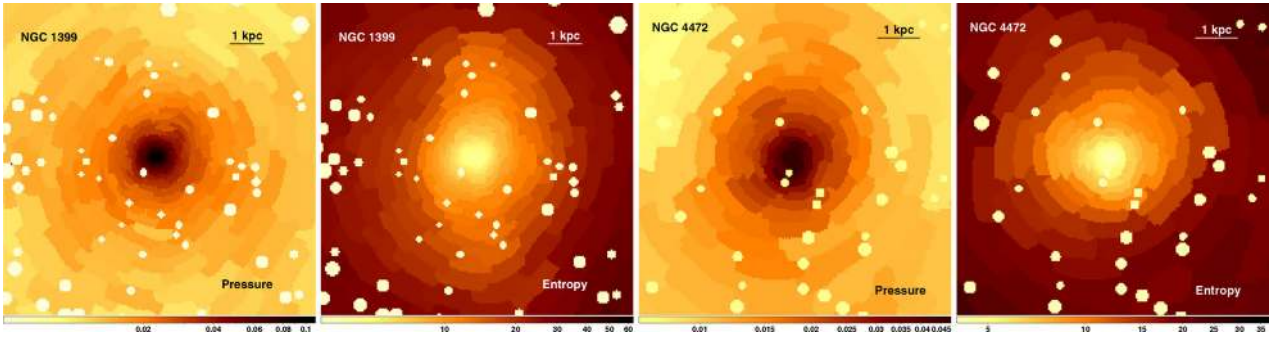
Figure 7. 2D maps of the hot gas pressure and entropy for the two galaxies with little or no [C II] emitting cold gas detected.

Table 5. Deprojected thermodynamic properties at $r \sim 0.5$ kpc.

| Galaxy	n_e (cm^{-3})	kT (keV)	P_e (keV cm^{-3})	K (keV cm^2)	t_{cool} (10^7 yr)
NGC 1399	0.167 ± 0.005	0.950 ± 0.009	0.158 ± 0.005	3.14 ± 0.07	4.6
NGC 4472	0.154 ± 0.008	0.860 ± 0.012	0.132 ± 0.007	2.99 ± 0.12	4.3
NGC 4636	0.072 ± 0.001	0.535 ± 0.020	0.039 ± 0.001	3.11 ± 0.07	5.2
NGC 5044	0.068 ± 0.005	0.582 ± 0.037	0.039 ± 0.004	3.51 ± 0.27	5.9
NGC 5813	0.074 ± 0.003	0.616 ± 0.041	0.046 ± 0.005	3.50 ± 0.31	5.7
NGC 5846	0.076 ± 0.006	0.677 ± 0.033	0.052 ± 0.005	3.77 ± 0.26	6.2
NGC 6868	0.072 ± 0.002	0.768 ± 0.036	0.055 ± 0.003	4.45 ± 0.22	7.8
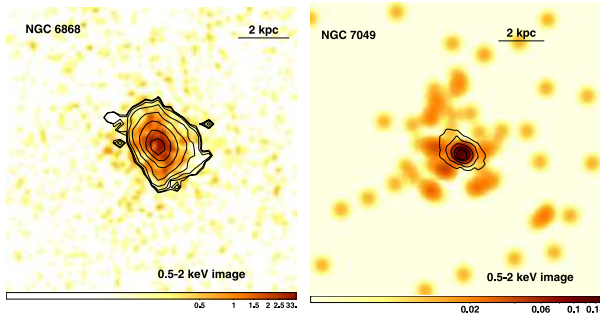
Figure 8. 0.5–2 keV *Chandra* images of the X-ray faintest galaxies in our sample, NGC 6868 and NGC 7049, with the Hα+[N II] contours overlaid. The statistical quality of the X-ray data does not allow us to produce 2D maps of thermodynamic properties for these two systems.

Figure 9. Entropy profiles for a sample of morphologically relaxed giant ellipticals (NGC 4472, NGC 1399, NGC 4649, NGC 1407, NGC 4261; Werner et al. 2012), with no extended optical emission-line nebulae (in black), and for five galaxies from our sample with [C II] emission indicating the presence of reservoirs of cold gas (NGC 5044, NGC 5813, NGC 5846, NGC 4636, NGC 6868 – in red). The entropy in galaxies containing cold gas is systematically lower at $r \gtrsim 1$ kpc. The only exception is NGC 6868 the entropy profile of which follows that of the cold-gas-poor galaxies.

form multiphase filaments where all the phases move together. The velocity structure measured in NGC 6868 and NGC 7049 indicates that the cold gas in these systems is distributed in large extended rotating discs. Given the expected densities of the [C II] emitting gas, its volume filling fraction must be low and the discs are also likely to be formed from many small clouds, sheets and filaments.

The observed velocity dispersions of the [C II] emitting gas are similar to the range of values measured from CO line widths and using optical and near-infrared integral field spectroscopy of 2000–10 000 K gas in the cooling cores of clusters (e.g. Edge 2001; Ogrean et al. 2010; Oonk et al. 2010; Farage, McGregor & Dopita 2012; Canning et al. 2013). Observations indicate that, due to their small volume filling fraction and large area covering factors, filaments may be blown about by the ambient hot gas, potentially serving as good tracers of its motions (Fabian et al. 2003). The measured velocity dispersions of the [C II] emitting gas, which reflect the range of velocities of the many small gas clouds/filaments moving through the galaxy, may therefore be indicative of the motions in the hot ISM. They are in general consistent with the limits and measurements
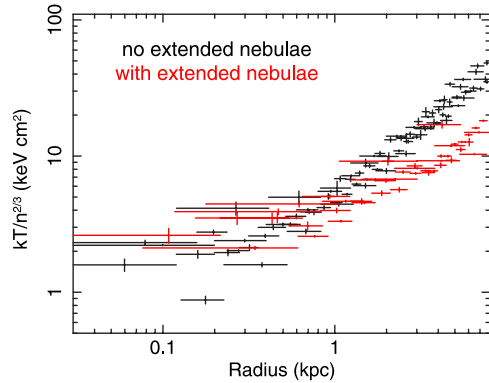
obtained through X-ray line broadening and resonant line scattering observations with the Reflection Grating Spectrometers on *XMM-Newton* (Werner et al. 2009; de Plaa et al. 2012; Sanders & Fabian 2013).

The MIR *Spitzer* spectra of all of our [C II] bright galaxies overlapping with the sample of Panuzzo et al. (2011) – NGC 4636, NGC 5044, NGC 5813, NGC 5846, NGC 6868 – show the presence of dust, warm H_2 molecular gas and for NGC 5044, NGC 6868 and NGC 4636 also polycyclic aromatic hydrocarbon (PAH) emission. Temi et al. (2007a) show that, for NGC 4472 and NGC 1399, galaxies with little or no [C II] detected, the infrared spectral energy distributions (SEDs) can be fully explained by circumstellar dust in the context of a steady-state model of dust production in normal

stellar mass loss followed by sputtering by the hot X-ray emitting gas. However, for all of the galaxies with extended [C II] emission, the infrared SEDs observed with *IRAS* and *Spitzer* indicate the presence of true interstellar dust, well in excess of the predictions of the steady-state model (Knapp et al. 1989; Temi et al. 2007a; Temi, Brighenti & Mathews 2007b). Although there are early reports of detections of H I emission in NGC 5846 and NGC 4636 (Bottinelli & Gouguenheim 1977, 1979; Knapp, Faber & Gallagher 1978), they were not confirmed by later re-observations (Krishna Kumar & Thonnard 1983; Lake & Schommer 1984; Knapp, Turner & Cunniffe 1985).

Werner et al. (2013) showed that the [S II] $\lambda6716/6731$ line ratios of the filaments in M87, indicate very low densities in the Hα+[N II] emitting 10 000 K phase. They concluded that, assuming subsonic turbulence in the filaments, the presence of significant magnetic pressure is required to keep this warm ionized gas in pressure equilibrium with the surrounding intracluster medium (ICM), indicating that the filaments are supported by magnetic fields of $B = 28$–73 μG. The assumption of subsonic turbulence is motivated by the lack of [O III] line emission, which would be produced by strong shocks. For 5/8 galaxies overlapping with the sample of Annibali et al. (2010), the [S II] $\lambda6717/6731$ line ratios point to very low densities, $n_e < 26$ cm^{-3}, in the ionized gas, indicating that it is supported by magnetic fields. Such low densities appear to be common in the ionized, extended emission-line nebulae in the cores of galaxy clusters. Significant magnetic fields threading the emission-line nebulae were also inferred using arguments based on the integrity of the filaments in the Perseus Cluster (Fabian et al. 2008) and based on radio observations of the Faraday rotation measure in cooling core clusters (Feretti et al. 1999; Allen et al. 2001; Taylor et al. 2001, 2007). This magnetic support may be slowing or preventing the gravitational collapse of any molecular gas clouds traced by the [C II] line emission that exceed the Jeans mass, preventing them from forming stars (e.g. see the discussion for NGC 1275 in Ho, Lim & Dinh-V-Trung 2009).

4.2 Heating and ionization of the cold ISM

In the six systems with significant cold gas mass reservoirs, the [C II] line emission appears to be cospatial with the Hα+[N II] emission, and with the lowest entropy X-ray emitting plasma. In the same galaxies, the ratios of [C II]/(Hα+[N II]) emission appear to be similar (0.4–0.8), indicating that in these systems the [C II] and Hα+[N II] emission are powered by the same energy source.

Photoionization by young hot stars or by the central AGN is negligible as a source of excitation for the nebulae in these galaxies. Ferland et al. (2009) showed that the broad-band emission-line spectra of the filamentary nebulae around central galaxies of cooling core clusters most likely originate in gas exposed to ionizing particles, either relativistic cosmic rays or hot X-ray emitting plasma penetrating into the cold gas. If the magnetized, ionized Hα emitting phase forms a thin skin on the underlying cold neutral gas, then the hot plasma particles must somehow overcome the obstacle presented by the magnetic fields. Based on the observations of the emission-line filaments in M87, Werner et al. (2010) and Werner et al. (2013) propose that shocks propagating within the hot X-ray emitting plasma as well as the movement of the filaments through this ambient hot gas (both as they are being uplifted and as they fall back) induce shearing around the filaments, thereby promoting mixing of the cold gas with the ambient hot medium via instabilities (e.g. Friedman, Heinz & Churazov 2012). Fabian et al. (2011) propose that the ionizing hot plasma in the core of the Perseus Cluster penetrates the cold filaments through magnetic reconnection diffu-

sion (Lazarian, Santos-Lima & de Gouveia Dal Pino 2010; Lazarian et al. 2011), which may be induced by shearing instabilities and turbulence. The penetration of the cold gas by the hot plasma particles implies that the X-ray emitting gas cools through mixing and thus the filaments of cold gas grow continuously in mass. If the mixing of the cold and hot gas phases turns more violent and the energy input rate due to penetrating hot plasma becomes larger than the cooling rate, this process may also lead to the destruction of the filaments.

On the other hand, according to the scenario proposed by Churazov, Ruszkowski & Schekochihin (2013), the filaments may be powered by the reconnection of the stretched magnetic fields in the wakes of AGN-inflated buoyantly rising bubbles, and do not necessarily grow in mass. The fact that the ratios of the [C II]/(Hα+[N II]) emission appear similar in both filamentary nebulae and rotating discs indicates that, despite the different morphologies, the gas is heated and ionized by the same energy source in both types of systems. But because the cold gas in the discy nebulae is not distributed in the wakes of AGN inflated bubbles, the scenario proposed by Churazov et al. (2013) could not explain their energy source. However, in the reconnection model, the powering of the cold gas could also be driven by the orbiting motion of the magnetized blobs/filaments through the hot plasma. This may lead to the sliding of the cold gas along the opposite-polarity magnetic fields and to the subsequent reconnection.

Despite its relatively low X-ray luminosity, the central pressure of the hot X-ray emitting plasma in the discy NGC 6868 is similar to the central pressures in the filamentary systems (see Table 5), indicating that in the absence of magnetic fields the heat flux from the hot into the cold phase would also be similar in both types of systems. It therefore appears that if the cold and hot phase come into direct contact – either due to turbulence, shearing motions or the magnetic fields tied to the ionized phase becoming unstable – hot gas particles penetrating into the cold gas provide a viable mechanism for powering the filaments in all of the systems in our sample. The penetrating particles will heat and increase the degree of ionization of the molecular gas clouds present within the filaments, increasing their Jeans mass and slowing down the collapse of the gas clouds in the presence of magnetic fields.

This model, calculated by Ferland et al. (2009) considering emission from an optically thin cell of gas, however, predicts [O I]/[C II] ~ 21, significantly higher than our observed range of 0.5–0.7. The ratios previously observed in the Perseus and Centaurus clusters, and in Abell 1068 and Abell 2597 are also low, in the range of 0.3–1 (Edge et al. 2010; Mittal et al. 2011, 2012). Mittal et al. (2012) conclude that these line ratios suggest that the lines are optically thick, implying a large reservoir of cold gas, which was not accounted for in previous inventories of the filament masses. Our measured ratios are consistent with the values determined previously in normal and starburst galaxies (Malhotra et al. 2001).

4.3 Origin of the cold ISM

A hotly debated question in the literature is whether the cold gas seen in the central giant elliptical galaxies in clusters and groups, and in early-type galaxies with X-ray haloes, originated from the radiative cooling of the hot plasma, from stellar mass loss, or whether it was accreted in mergers with gas-rich galaxies.

The difference between the entropy profiles of the systems with cool gas and those without it in Fig. 9 supports the argument that the cold gas originates by cooling from the hot phase. In more massive clusters, Hα filaments are always cospatial with soft X-ray

emitting ~ 0.5 keV gas (Sanders & Fabian 2007; Sanders et al. 2008, 2009, 2010; de Plaa et al. 2010; Werner et al. 2010, 2011, 2013), indicating that the cold gas must be related to the hot phase. Furthermore, significant star formation and line emitting gas around the central galaxy are only found in systems where the central cooling time is short, or, equivalently, the central entropy is low (Rafferty, McNamara & Nulsen 2008; Cavagnolo et al. 2008).

The parameter

$$\Pi_{\mathrm{F}} = \frac{\kappa T}{n_e n_{\mathrm{H}} \Lambda(T) r^2}, \qquad (2)$$

where κ is the thermal conductivity, T is the temperature, Λ is the cooling function, and n_e and n_{H} are the electron and hydrogen number densities, respectively, is a measure of the ratio of the conductive heating rate to the radiative cooling rate on scales comparable to r, i.e. the 'Field criterion' for thermal instability (Field 1965). Fig. 10 shows the Field criterion, Π_{F}, as a function of the radius, where the systems with substantial quantities of cold gas are plotted in red. There is a clear dichotomy with the cold-gas-rich systems remaining unstable out to relatively large radii. This result strongly indicates that the cold gas is produced chiefly by thermally unstable cooling from the hot phase. A similar result was found for a sample of central galaxies in more massive clusters by Voit et al. (2008), who found minimum values of $\Pi_{\mathrm{F}} \lesssim 5$ in all systems with star formation. Voit et al. (2008) argued that the effective conductivity is suppressed by a factor of about 5 by magnetic fields, in which case all of their systems with young stars are thermally unstable by the Field criterion.

The Field criterion alone is insufficient to ensure that the gas is thermally unstable. In a spherical atmosphere, the gas is supported by buoyancy, so that an overdense blob tends to fall inwards on the free-fall time-scale towards its equilibrium position where the surrounding gas has the same specific entropy and requires the same specific heating rate. This suppresses the growth of thermal instability unless the cooling time is comparable to the free-fall time or shorter (Cowie, Fabian & Nulsen 1980; Balbus & Soker 1989). Using numerical simulations, Sharma et al. (2012) found that thermal instability is only significant when the cooling time is less than ~ 10 free-fall times (see also Gaspari, Ruszkowski & Sharma

2012; Kunz et al. 2012; McCourt et al. 2012; Gaspari, Ruszkowski & Oh 2013). However, this condition can be circumvented if an overdense gas blob is prevented from falling to its equilibrium position by the magnetic fields which pin the cloud to the ambient ICM (Nulsen 1986), or by rotational support in addition to buoyancy.

If a cooling cloud has sufficient angular momentum that is retained while it cools, it can cool unstably on to a non-radial orbit. This provides an alternative condition for thermal instability, that the viscous diffusion length in a cooling time, $\sqrt{\nu t_c}$, where ν is the kinematic viscosity and t_c is the cooling time, must be smaller than the size of a cloud. Analogous to the Field criterion, we define the stability parameter

$$\Pi_{\mathrm{v}} = \frac{\nu t_c}{r^2}, \qquad (3)$$

which needs to be smaller than about unity for thermal instability to develop on scales comparable to r. Viscous stresses in a plasma (Braginskii 1965) are much less sensitive to the structure of the magnetic field than conduction (e.g. Nulsen & McNamara 2013) and, although the stresses have a different tensor character in magnetized and unmagnetized plasmas, the viscosity itself is the same. Because the underlying process is diffusion controlled by Coulomb collisions in both cases (electrons for Π_{F} and ions for Π_{v}), the ratio of these two parameters is almost constant at $\Pi_{\mathrm{v}}/\Pi_{\mathrm{F}} \simeq 0.0253$. Numerical simulations are needed to determine a more accurate stability threshold, but we expect that the viscous diffusion length needs to be somewhat smaller than r for instability by this mechanism. The condition $\Pi_{\mathrm{F}} < 5$ translates to $\Pi_{\mathrm{v}} \lesssim 0.13$, or the diffusion length in one cooling time being $\lesssim 0.36r$. Although it is unclear which stability threshold takes precedence, we conclude that it is sufficient to test only one of these parameters, which we take to be Π_{F}, for stability.

Our *Herschel* data reveal that in two galaxies, NGC 6868 and NGC 7049, the cold gas forms rotating discs with radii $r \sim 3$ kpc. The discs of cold gas in these systems rotate with orbital velocities of up to 250 km s^{-1}. If this gas cooled from the hot phase, its rotation implies that the hot atmospheres of these systems have significant net angular momentum and the hot gas cools on to non-radial orbits. In the case of NGC 6868, this angular momentum may have been provided by gas sloshing indicated by the *Chandra* data (Machacek et al. 2010). Because the atmosphere is aspherical, heating originating from the centre of the galaxy cannot balance the cooling rate locally throughout the atmosphere and so should not be expected to stop hot gas from cooling on to an extended disc. Because of this, and because rotational support prevents infall, instabilities may develop more easily and the gas may become thermally unstable at higher Π_{F} than in non-rotating systems. This is consistent with our results presented in Fig. 10, where Π_{F} for NGC 6868, shown with a dashed line, is higher than Π_{F} for the other systems containing non-rotating cold gas. The Field criterion still needs to be met, but the behaviour of the stability parameter in NGC 6868 also indicates that the viscous stability criterion takes precedence.

However, in the context of the radiative cooling model, the presence of dust and PAHs within the cold gas clouds (Panuzzo et al. 2011) is intriguing. It suggests that at least some of the cold material originated from stellar mass loss (see also Donahue et al. 2011; Voit & Donahue 2011, for galaxy clusters). Our understanding of dust formation is, however, limited and it cannot be ruled out that dust may somehow form within the cold gas clouds (Fabian, Johnstone & Daines 1994). Recent *Herschel* observations suggest that in the most massive galaxies, the dust mass is unconnected to the stellar
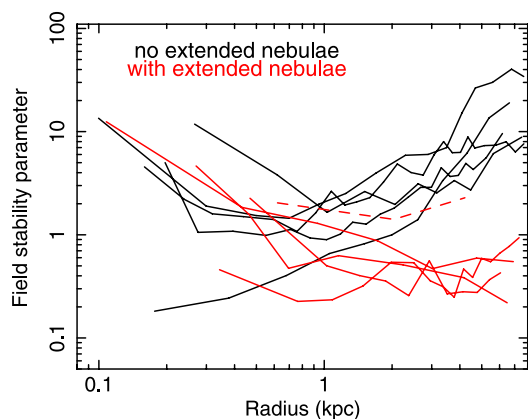

Figure 10. The Field criterion, $\Pi_{\mathrm{F}} = \kappa T / (n_e n_{\mathrm{H}} \Lambda(T) r^2)$, as a function of radius for the galaxies that display extended emission-line nebulae and [C II] line emission (shown in red) and for a sample of arguably cold-gas-poor systems (shown in black). The clear dichotomy, with the cold-gas-rich systems being thermally unstable out to relatively large radii, indicates that the cold gas originates from the cooling hot phase. The galaxy NGC 6868, which shows evidence for a rotating disc of gas, is shown with a dashed line.

populations, leading to the suggestion that the dust and the cold gas in these systems have been acquired externally (Smith et al. 2012). Rawle et al. (2012) show that the dust-to-stellar mass ratios in BCGs without line emitting nebulae are much smaller than in systems with cold gas. In the absence of cold gas clouds, the dust produced by stellar mass loss will get destroyed by sputtering and the tenuous gas, lost by stars, may get more easily mixed with and assimilated into the hot ISM. Therefore, if a galaxy loses all of its cold gas content (e.g. due to AGN activity), then stellar mass loss will likely become inefficient in rebuilding its cold gas reservoir. A galaxy that loses its cold gas content will therefore remain free of gas and dust until it again accretes cold material from the cooling hot phase or in a wet merger. This may have happened to NGC 1399 and NGC 4472. On the other hand, if a galaxy already contains clouds of cold gas (it either never lost its cold ISM or it accreted some cold material externally), then these clouds and filaments will help preserving the products of stellar mass loss (both the gas and the dust) by assimilating them as they plough through the galaxy.

In the systems with filamentary cold gas, the AGN jets and the buoyant bubbles of relativistic plasma seem to interact with the filaments, dragging them out from the centre of the galaxy. As these filaments move through the hot ISM they may get penetrated by hot particles, which deposit energy into the cold gas heating and ionizing it. This interaction can both destroy the cold gas and contribute to the growth of its mass, depending on the energy input rate from the hot into the cold phase. In the context of this model, the total gas/dust mass will not correlate with the stellar mass of the galaxy, but it will depend on the balance between heating and cooling and on the interaction of the cold nebulae with the AGN (see also Mathews et al. 2013).

4.4 Fuelling the AGN

The jet powers, determined from the work required to inflate bubbles of relativistic plasma associated with the cavities in the hot X-ray emitting atmospheres, do not increase with the amount of cold gas in these galaxies. On the contrary, the two galaxies that lack any significant reservoirs of cold gas have the largest jet powers in our sample. These galaxies, NGC 1399 and NGC 4472, also have the largest hot ISM densities in their cores. Accretion of hot gas in galaxies with high core densities can naturally result in higher jet powers, as has been demonstrated by the correlation between the Bondi accretion rates of hot gas and the observed jet powers in such ellipticals (Allen et al. 2006). The pressure and entropy distributions of the hot ISM in the cores of these two galaxies look remarkably regular, with the X-ray cavities/radio-lobes appearing at larger radii of ∼4 and ∼8 kpc for NGC 4472 and NGC 1399, respectively.

Other nearby giant elliptical galaxies that appear morphologically relaxed in their cores, such as NGC 4649, NGC 1407, NGC 4261 or NGC 1404, also do not display extended optical emission-line nebulae (Macchetto et al. 1996; Baldi et al. 2009; Tremblay et al. 2009; Moustakas et al. 2010), indicating that they too are relatively depleted of cold gas. Interestingly, some of these morphologically relaxed cold-gas-poor systems, such as NGC 4261, have very large jet powers, with jets puncturing through the X-ray emitting galactic atmosphere to form giant lobes in the surrounding intragroup medium (O'Sullivan et al. 2011). For others, such as NGC 1404, NGC 4649 and NGC 1407, however, the current jet powers are more modest (Shurkin et al. 2008; Giacintucci et al. 2012).

Galaxies containing large reservoirs of cold gas, on the other hand, in general display strongly disturbed X-ray morphologies, possibly relating to earlier AGN outbursts impacting the cores of these systems. In principle, the presence of cold gas may affect both accretion and jet heating in these systems. Accretion of clumpy multiphase gas (hot plasma mixed with cooler, filamentary gas) may result in variable accretion rates and power output of the AGN jets, potentially triggering sporadic, larger outbursts than would be typical from the steady accretion of hot gas alone. Because of the relatively small volume filling fraction of this cooler gas, these outbursts may be relatively short (arguments for sporadic cold/multiphase accretion in radio-mode AGN in galaxy clusters have also been presented by Rafferty et al. 2006; Russell et al. 2013b).

As demonstrated by Morganti et al. (2013), radio-mechanical feedback does not only operate on the hot tenuous atmospheres of galaxies but also on the dense cold gas, which can be accelerated by jets to high speeds. Recent observations using ALMA also show that radio-mode AGN activity can drive massive outflows of molecular gas from BCGs (McNamara et al. 2013; Russell et al. 2013a). In systems with large cold gas reservoirs, jets may be more easily slowed by coupling to this material, and may therefore deposit most of their energy at smaller radii. This will result in more disturbed central thermodynamic distributions and, in particular, may decrease the central hot ISM density, resulting in lower hot gas accretion rates between the relatively brief periods of multiphase accretion. Any reduction in the accretion rates from the hot gas would result in smaller jet powers, consistent with the observations presented here.

Numerical simulations (Wagner & Bicknell 2011; Wagner, Bicknell & Umemura 2012) have shown that radio jets can be efficient in clearing the central regions of galaxies of their cold gas, provided that the cold gas clouds are porous, clumpy and have small volume filling fractions, with individual clouds being relatively small, which again are characteristics consistent with the observations discussed here. Powerful jets may thus eventually destroy or remove most of the cold gas in the cores of the galaxies, allowing the jets to propagate further out and deposit their energy at larger radii, increasing the entropy of the hot galactic atmospheres. This in turn will allow the density of the hot gas in the core of the galaxy to increase, thus increasing the jet power. The central regions of galaxies cleared of cold gas may acquire relaxed morphologies within the central $r \sim 5$ kpc over $\sim 5 \times 10^7$ yr or a few sound crossing times. The similarity of the thermodynamic profiles of elliptical galaxies with highly relaxed X-ray morphologies (see the black data points in Fig. 9 and Werner et al. 2012) indicates that, after elliptical galaxies are cleared of cold gas, jet heating and cooling of their hot atmospheres comes to an equilibrium in an approximately universal manner. The galaxies may maintain these equilibria until they are disturbed by a merger event.

5 CONCLUSIONS

Using FIR, optical and X-ray data, we study the ISM in eight nearby, X-ray and optically bright, giant elliptical galaxies, all central dominant members of relatively low-mass groups. We find that:

(i) All systems with extended Hα emission in our sample (6/8 galaxies) display significant [C II] line emission that traces ∼100 K gas.

(ii) This emission is cospatial with the optical Hα+[N II] emitting nebulae and the lowest entropy soft X-ray emitting plasma.

(iii) These systems have similar [C II]/(Hα+[N II]) ratios of 0.4–0.8, indicating that the [C II] and Hα+[N II] emission are powered

by the same energy source. The likely dominant source of energy is the hot X-ray emitting plasma penetrating into the cold gas.

(iv) The entropy profiles of the hot galactic atmospheres show a clear dichotomy, with the systems displaying extended emission-line nebulae having lower entropies beyond $r \gtrsim 1$ kpc than the cold-gas-poor systems. We show that while the hot atmospheres of the cold-gas-poor galaxies are thermally stable outside of their innermost cores, the atmospheres of the cold-gas-rich systems are prone to cooling instabilities. This provides considerable weight to the argument that cold gas in giant ellipticals is produced chiefly by cooling from the hot phase. We show that cooling instabilities may develop more easily in rotating systems and discuss an alternative condition for thermal instability for this case.

(v) The hot atmospheres of cold-gas-rich galaxies display disturbed morphologies indicating that the accretion of clumpy multiphase gas in these systems may result in variable power output of the AGN jets, potentially triggering sporadic, larger outbursts. The jets may be more easily slowed by coupling to the dense cold material and may therefore deposit most of their energy at smaller radii, resulting in the observed disturbed central thermodynamic distributions.

(vi) In the two cold-gas-poor, X-ray morphologically relaxed galaxies of our sample, NGC 1399 and NGC 4472, powerful AGN outbursts may have destroyed or removed most of the cold gas from the cores, allowing the jets to propagate and deposit most of their energy further out, increasing the entropy of the hot galactic atmospheres and leaving their cores relatively undisturbed. These observations indicate that radio-mechanical AGN feedback is likely to play a crucial role in clearing giant elliptical galaxies of their cold gas, keeping them 'red and dead'.

ACKNOWLEDGEMENTS

REFERENCES

Allen S. W. et al., 2001, MNRAS, 324, 842
Allen S. W., Dunn R. J. H., Fabian A. C., Taylor G. B., Reynolds C. S., 2006, MNRAS, 372, 21
Annibali F., Bressan A., Rampazzo R., Zeilinger W. W., Danese L., 2007, A&A, 463, 455
Annibali F., Bressan A., Rampazzo R., Zeilinger W. W., Vega O., Panuzzo P., 2010, A&A, 519, A40
Arnaud K. A., 1996, in Jacoby G. H., Barnes J., eds, ASP Conf. Ser. Vol. 101, Astronomical Data Analysis Software and Systems V. Astron. Soc. Pac., San Francisco, p. 17
Balbus S. A., Soker N., 1989, ApJ, 341, 611
Baldi A., Forman W., Jones C., Kraft R., Nulsen P., Churazov E., David L., Giacintucci S., 2009, ApJ, 707, 1034
Blakeslee J. P. et al., 2009, ApJ, 694, 556

Bondi H., 1952, MNRAS, 112, 195
Bottinelli L., Gouguenheim L., 1977, A&A, 60, L23
Bottinelli L., Gouguenheim L., 1979, A&A, 74, 172
Braginskii S. I., 1965, Rev. Plasma Phys., 1, 205
Buson L. M. et al., 1993, A&A, 280, 409
Canning R. E. A. et al., 2013, MNRAS, 435, 1108
Caon N., Macchetto D., Pastoriza M., 2000, ApJS, 127, 39
Cavagnolo K. W., Donahue M., Voit G. M., Sun M., 2008, ApJ, 683, L107
Churazov E., Sunyaev R., Forman W., Böhringer H., 2002, MNRAS, 332, 729
Churazov E., Ruszkowski M., Schekochihin A., 2013, MNRAS, 436, 526
Condon J. J., Cotton W. D., Greisen E. W., Yin Q. F., Perley R. A., Taylor G. B., Broderick J. J., 1998, AJ, 115, 1693
Condon J. J., Cotton W. D., Broderick J. J., 2002, AJ, 124, 675
Cowie L. L., Fabian A. C., Nulsen P. E. J., 1980, MNRAS, 191, 399
Cowie L. L., Hu E. M., Jenkins E. B., York D. G., 1983, ApJ, 272, 29
Crawford M. K., Genzel R., Townes C. H., Watson D. M., 1985, ApJ, 291, 755
Crawford C. S., Allen S. W., Ebeling H., Edge A. C., Fabian A. C., 1999, MNRAS, 306, 857
Croton D. J. et al., 2006, MNRAS, 365, 11
David L. P., Jones C., Forman W., Nulsen P., Vrtilek J., O'Sullivan E., Giacintucci S., Raychaudhury S., 2009, ApJ, 705, 624
David L. P. et al., 2011, ApJ, 728, 162
de Plaa J., Werner N., Simionescu A., Kaastra J. S., Grange Y. G., Vink J., 2010, A&A, 523, A81
de Plaa J., Zhuravleva I., Werner N., Kaastra J. S., Churazov E., Smith R. K., Raassen A. J. J., Grange Y. G., 2012, A&A, 539, A34
Donahue M., Stocke J. T., Gioia I. M., 1992, ApJ, 385, 49
Donahue M., Mack J., Voit G. M., Sparks W., Elston R., Maloney P. R., 2000, ApJ, 545, 670
Donahue M., de Messières G. E., O'Connell R. W., Voit G. M., Hoffer A., McNamara B. R., Nulsen P. E. J., 2011, ApJ, 732, 40
Dunn R. J. H., Allen S. W., Taylor G. B., Shurkin K. F., Gentile G., Fabian A. C., Reynolds C. S., 2010, MNRAS, 404, 180
Edge A. C., 2001, MNRAS, 328, 762
Edge A. C., Frayer D. T., 2003, ApJ, 594, L13
Edge A. C., Wilman R. J., Johnstone R. M., Crawford C. S., Fabian A. C., Allen S. W., 2002, MNRAS, 337, 49
Edge A. C. et al., 2010, A&A, 518, L46
Fabian A. C., Johnstone R. M., Daines S. J., 1994, MNRAS, 271, 737
Fabian A. C., Sanders J. S., Crawford C. S., Conselice C. J., Gallagher J. S., Wyse R. F. G., 2003, MNRAS, 344, L48
Fabian A. C., Johnstone R. M., Sanders J. S., Conselice C. J., Crawford C. S., Gallagher J. S., III, Zweibel E., 2008, Nature, 454, 968
Fabian A. C., Sanders J. S., Williams R. J. R., Lazarian A., Ferland G. J., Johnstone R. M., 2011, MNRAS, 417, 172
Falcke H., Rieke M. J., Rieke G. H., Simpson C., Wilson A. S., 1998, ApJ, 494, L155
Farage C. L., McGregor P. J., Dopita M. A., 2012, ApJ, 747, 28
Feretti L., Dallacasa D., Govoni F., Giovannini G., Taylor G. B., Klein U., 1999, A&A, 344, 472
Ferland G. J., Fabian A. C., Hatch N. A., Johnstone R. M., Porter R. L., van Hoof P. A. M., Williams R. J. R., 2009, MNRAS, 392, 1475
Field G. B., 1965, ApJ, 142, 531
Friedman S. H., Heinz S., Churazov E., 2012, ApJ, 746, 112
Gaspari M., Ruszkowski M., Sharma P., 2012, ApJ, 746, 94
Gaspari M., Ruszkowski M., Oh S. P., 2013, MNRAS, 432, 3401
Gastaldello F., Buote D. A., Temi P., Brighenti F., Mathews W. G., Ettori S., 2009, ApJ, 693, 43
Giacintucci S. et al., 2012, ApJ, 755, 172
Goudfrooij P., Hansen L., Jorgensen H. E., Norgaard-Nielsen H. U., 1994, A&AS, 105, 341
Hao C.-N., Kennicutt R. C., Johnson B. D., Calzetti D., Dale D. A., Moustakas J., 2011, ApJ, 741, 124
Hatch N. A., Crawford C. S., Fabian A. C., Johnstone R. M., 2005, MNRAS, 358, 765

Hatch N. A., Crawford C. S., Johnstone R. M., Fabian A. C., 2006, MNRAS, 367, 433

Heckman T. M., Baum S. A., van Breugel W. J. M., McCarthy P., 1989, ApJ, 338, 48

Ho I.-T., Lim J., Dinh-V-Trung, 2009, ApJ, 698, 1191

Jaffe W., Bremer M. N., 1997, MNRAS, 284, L1

Jaffe W., Bremer M. N., Baker K., 2005, MNRAS, 360, 748

Jarrett T. H., Chester T., Cutri R., Schneider S. E., Huchra J. P., 2003, AJ, 125, 525

Johnstone R. M., Fabian A. C., Nulsen P. E. J., 1987, MNRAS, 224, 75

Johnstone R. M., Hatch N. A., Ferland G. J., Fabian A. C., Crawford C. S., Wilman R. J., 2007, MNRAS, 382, 1246

Kaastra J. S., Mewe R., Nieuwenhuijzen H., 1996, in Yamashita K., Watanabe T., eds, Proc. 11th Colloq. on UV and X-ray Spectroscopy of Astrophysical and Laboratory Plasmas, SPEX: A New Code for Spectral Analysis of X and UV Spectra. Universal Academy Press, Tokyo, p. 411

Kalberla P. M. W., Burton W. B., Hartmann D., Arnal E. M., Bajaja E., Morras R., Pöppel W. G. L., 2005, A&A, 440, 775

Knapp G. R., Faber S. M., Gallagher J. S., 1978, AJ, 83, 11

Knapp G. R., Turner E. L., Cunniffe P. E., 1985, AJ, 90, 454

Knapp G. R., Guhathakurta P., Kim D.-W., Jura M. A., 1989, ApJS, 70, 329

Krishna Kumar C., Thonnard N., 1983, AJ, 88, 260

Kunz M. W., Bogdanović T., Reynolds C. S., Stone J. M., 2012, ApJ, 754, 122

Lake G., Schommer R. A., 1984, ApJ, 280, 107

Lazarian A., Santos-Lima R., de Gouveia Dal Pino E., 2010, in Pogorelov N. V., Audit E., Zank G. P., eds, ASP Conf. Ser. Vol. 429, Numerical Modelling of Space Plasma Flows, Astronum-2009. Astron. Soc. Pac., San Francisco, p. 113

Lazarian A., Kowal G., Vishniac E., de Gouveia Dal Pino E., 2011, Planet. Space Sci., 59, 537

Lim J., Ohyama Y., Chi-Hung Y., Dinh-V-Trung, Shiang-Yu W., 2012, ApJ, 744, 112

Macchetto F., Pastoriza M., Caon N., Sparks W. B., Giavalisco M., Bender R., Capaccioli M., 1996, A&AS, 120, 463

McCourt M., Sharma P., Quataert E., Parrish I. J., 2012, MNRAS, 419, 3319

McDonald M., Veilleux S., Rupke D. S. N., Mushotzky R., 2010, ApJ, 721, 1262

McDonald M., Wei L. H., Veilleux S., 2012, ApJ, 755, L24

Machacek M. E., O'Sullivan E., Randall S. W., Jones C., Forman W. R., 2010, ApJ, 711, 1316

McNamara B. R. et al., 2013, ApJ, preprint (arXiv:1309.0013)

Magorrian J. et al., 1998, AJ, 115, 2285

Malhotra S. et al., 2001, ApJ, 561, 766

Mathews W. G., Temi P., Brighenti F., Amblard A., 2013, ApJ, 768, 28

Million E. T., Allen S. W., Werner N., Taylor G. B., 2010a, MNRAS, 405, 1624

Million E. T., Werner N., Simionescu A., Allen S. W., Nulsen P. E. J., Fabian A. C., Böhringer H., Sanders J. S., 2010b, MNRAS, 407, 2046

Mittal R. et al., 2011, MNRAS, 418, 2386

Mittal R. et al., 2012, MNRAS, 426, 2957

Morganti R., Fogasy J., Paragi Z., Oosterloo T., Orienti M., 2013, Science, 341, 1082

Moustakas J., Kennicutt R. C., Jr, Tremonti C. A., Dale D. A., Smith J.-D. T., Calzetti D., 2010, ApJS, 190, 233

Nulsen P. E. J., 1986, MNRAS, 221, 377

Nulsen P. E. J., McNamara B. R., 2013, Astron. Nachr., 334, 386

O'Sullivan E., Forbes D. A., Ponman T. J., 2001, MNRAS, 328, 461

O'Sullivan E., Worrall D. M., Birkinshaw M., Trinchieri G., Wolter A., Zezas A., Giacintucci S., 2011, MNRAS, 416, 2916

O'Sullivan E., David L. P., Vrtilek J. M., 2013, MNRAS, 437, 730

Ogrean G. A., Hatch N. A., Simionescu A., Böhringer H., Brüggen M., Fabian A. C., Werner N., 2010, MNRAS, 406, 354

Oonk J. B. R., Jaffe W., Bremer M. N., van Weeren R. J., 2010, MNRAS, 405, 898

Panuzzo P., Rampazzo R., Bressan A., Vega O., Annibali F., Buson L. M., Clemens M. S., Zeilinger W. W., 2011, A&A, 528, A10

Pilbratt G. L. et al., 2010, A&A, 518, L1

Poglitsch A. et al., 2010, A&A, 518, L2

Rafferty D. A., McNamara B. R., Nulsen P. E. J., Wise M. W., 2006, ApJ, 652, 216

Rafferty D. A., McNamara B. R., Nulsen P. E. J., 2008, ApJ, 687, 899

Randall S. W. et al., 2011, ApJ, 726, 86

Rawle T. D. et al., 2012, ApJ, 747, 29

Rickes M. G., Pastoriza M. G., Bonatto C., 2004, A&A, 419, 449

Russell H. R. et al., 2013a, ApJ, preprint (arXiv:1309.0014)

Russell H. R., McNamara B. R., Edge A. C., Hogan M. T., Main R. A., Vantyghem A. N., 2013b, MNRAS, 432, 530

Salomé P., Combes F., 2003, A&A, 412, 657

Sanders J. S., 2006, MNRAS, 371, 829

Sanders J. S., Fabian A. C., 2007, MNRAS, 381, 1381

Sanders J. S., Fabian A. C., 2013, MNRAS, 429, 2727

Sanders J. S., Fabian A. C., Allen S. W., Morris R. G., Graham J., Johnstone R. M., 2008, MNRAS, 385, 1186

Sanders J. S., Fabian A. C., Taylor G. B., 2009, MNRAS, 396, 1449

Sanders J. S., Fabian A. C., Frank K. A., Peterson J. R., Russell H. R., 2010, MNRAS, 402, 127

Schure K. M., Kosenko D., Kaastra J. S., Keppens R., Vink J., 2009, A&A, 508, 751

Sharma P., McCourt M., Quataert E., Parrish I. J., 2012, MNRAS, 420, 3174

Shurkin K., Dunn R. J. H., Gentile G., Taylor G. B., Allen S. W., 2008, MNRAS, 383, 923

Sijacki D., Springel V., Di Matteo T., Hernquist L., 2007, MNRAS, 380, 877

Silk J., Rees M. J., 1998, A&A, 331, L1

Smith M. W. L. et al., 2012, ApJ, 748, 123

Sparks W. B. et al., 2012, ApJ, 750, L5

Stacey G. J., Geis N., Genzel R., Lugten J. B., Poglitsch A., Sternberg A., Townes C. H., 1991, ApJ, 373, 423

Sun M., Donahue M., Voit G. M., 2007, ApJ, 671, 190

Taylor G. B., Govoni F., Allen S. W., Fabian A. C., 2001, MNRAS, 326, 2

Taylor G. B., Fabian A. C., Gentile G., Allen S. W., Crawford C., Sanders J. S., 2007, MNRAS, 382, 67

Temi P., Brighenti F., Mathews W. G., 2007a, ApJ, 660, 1215

Temi P., Brighenti F., Mathews W. G., 2007b, ApJ, 666, 222

Tonry J. L., Dressler A., Blakeslee J. P., Ajhar E. A., Fletcher A. B., Luppino G. A., Metzger M. R., Moore C. B., 2001, ApJ, 546, 681

Tremblay G. R. et al., 2009, ApJS, 183, 278

Voit G. M., Donahue M., 2011, ApJ, 738, L24

Voit G. M., Cavagnolo K. W., Donahue M., Rafferty D. A., McNamara B. R., Nulsen P. E. J., 2008, ApJ, 681, L5

Wagner A. Y., Bicknell G. V., 2011, ApJ, 728, 29

Wagner A. Y., Bicknell G. V., Umemura M., 2012, ApJ, 757, 136

Werner N., Zhuravleva I., Churazov E., Simionescu A., Allen S. W., Forman W., Jones C., Kaastra J. S., 2009, MNRAS, 398, 23

Werner N. et al., 2010, MNRAS, 407, 2063

Werner N. et al., 2011, MNRAS, 415, 3369

Werner N., Allen S. W., Simionescu A., 2012, MNRAS, 425, 2731

Werner N. et al., 2013, ApJ, 767, 153
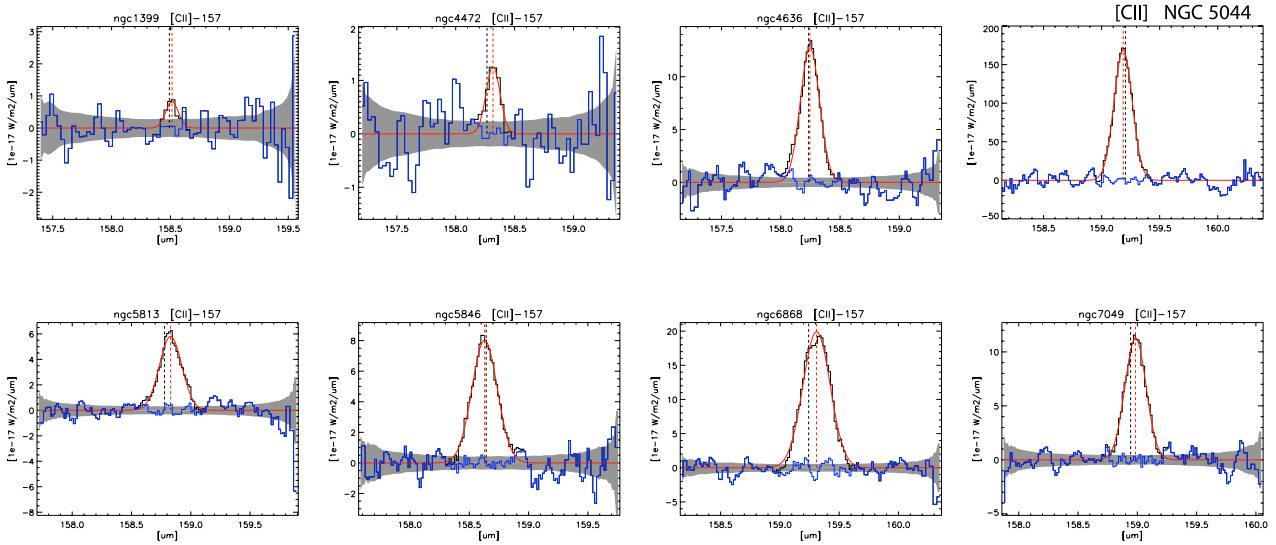
APPENDIX A: PLOTS OF THE FIR LINE SPECTRA

Figure A1. The FIR [C II] λ157 μm line obtained from the central spaxel (9.4 × 9.4 arcsec²) of the *Herschel* PACS rebinned data cube, except for NGC 5044 where the spectrum was obtained from an 80 × 80 arcsec wide box. The spectra for NGC 1399 and NGC 4472 were re-binned in wavelength. The blue line indicates the residuals between the data and the model. The grey shaded area indicates the detector noise. No reliable noise product is available for the raster scan data of NGC 5044. The red and black dashed lines show the expected (for gas at rest at the redshift of the galaxy) and the observed best-fitting line centroids, respectively.
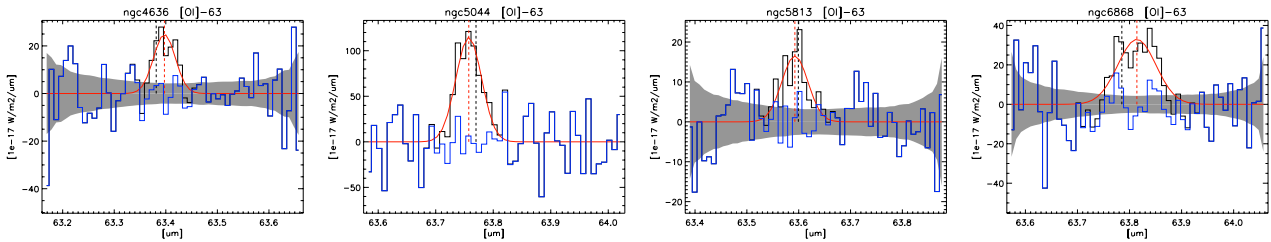
Figure A2. The FIR [O I] λ63.2 μm line obtained from the central spaxel (9.4 × 9.4 arcsec²) of the *Herschel* PACS rebinned data cube, except for NGC 5044 where the spectrum was obtained from a 24 arcsec wide box. The spectra were re-binned in wavelength. The blue line indicates the residuals between the data and the model. The grey shaded area indicates the detector noise. No reliable noise product is available for the raster scan data of NGC 5044. Because the noise is a strong function of the wavelength, increasing towards the edges of the observed wavelength band, the noise in the adjacent bands may reach an amplitude that is comparable to that of the spectral lines, with the lines still remaining statistically significant. The red and black dashed lines show the expected (for gas at rest at the redshift of the galaxy) and the observed best-fitting line centroids, respectively.
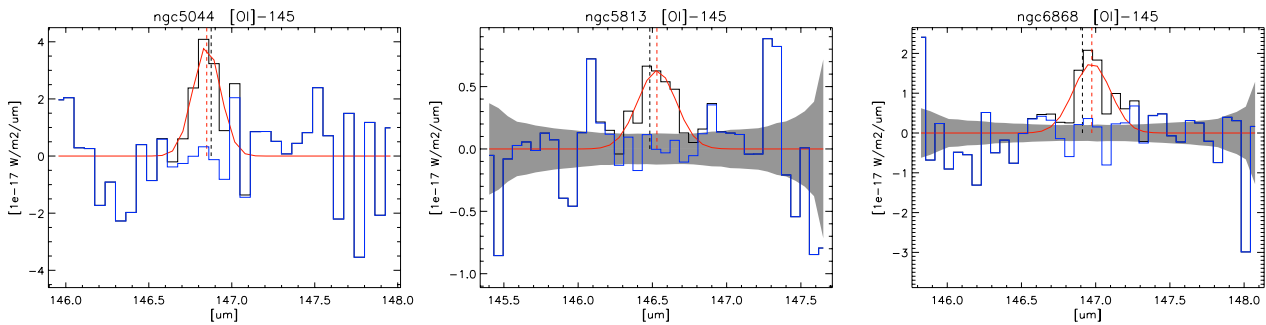
Figure A3. The FIR [O Ib] λ145.5 μm line obtained from the central spaxel (9.4 × 9.4 arcsec²) of the *Herschel* PACS rebinned data cube, except for NGC 5044 where the spectrum was obtained from a 24 arcsec wide box. The spectra were re-binned in wavelength. The blue line indicates the residuals between the data and the model. The grey shaded area indicates the detector noise. No reliable noise product is available for the raster scan data of NGC 5044. Because the noise is a strong function of the wavelength, increasing towards the edges of the observed wavelength band, the noise in the adjacent bands may reach an amplitude that is comparable to that of the spectral lines, with the lines still remaining statistically significant. The red and black dashed lines show the expected (for gas at rest at the redshift of the galaxy) and the observed best-fitting line centroids, respectively.

This paper has been typeset from a TEX/LATEX file prepared by the author.